Longshore Sediment Transport Across a Tombolo Determined by Two Adjacent Circulation Cells

Journal of Geophysical Research: Earth Surface

Xie, Danghan; Hughes, Zoe; FitzGerald, Duncan; Tas, Silke; Asik, Tansir Zaman et al

https://doi.org/10.1029/2024JF007709

JGR Earth Surface

RESEARCH ARTICLE
10.1029/2024JF007709

Longshore Sediment Transport Across a Tombolo Determined by Two Adjacent Circulation Cells

Danghan Xie[1,2], Zoe Hughes[1], Duncan FitzGerald[1], Silke Tas[1,3], Tansir Zaman Asik[1], and Sergio Fagherazzi[1]

[1]Department of Earth and Environment, Boston University, Boston, MA, USA, [2]Scripps Institution of Oceanography, University of California San Diego, La Jolla, CA, USA, [3]Hydrology and Environmental Hydraulics, Wageningen University and Research, Wageningen, the Netherlands

Key Points:

- The position, magnitude, and size of circulation cells on both sides of a tombolo vary with storm surge, wave height, and wave direction
- Circulation cells and storm-driven water level differences determine sediment transport across the tombolo
- Longshore sediment transport across the tombolo is negligible except during extreme storms

Supporting Information:

Supporting Information may be found in the online version of this article.

Correspondence to:

D. Xie,
danghan@ucsd.edu

Citation:

Xie, D., Hughes, Z., FitzGerald, D., Tas, S., Asik, T. Z., & Fagherazzi, S. (2024). Longshore sediment transport across a tombolo determined by two adjacent circulation cells. *Journal of Geophysical Research: Earth Surface*, *129*, e2024JF007709. https://doi.org/10.1029/2024JF007709

Received 26 FEB 2024
Accepted 15 SEP 2024

Abstract Longshore sediment transport (LST) is essential for shaping sandy shorelines. Many shorelines are complex and indented, containing headlands, offshore islands and tombolos. Tombolos often form between islands and the mainland; however, the conditions for LST across tombolos are unclear. This question is important because tombolos are often reinforced with anthropogenic infrastructure, potentially causing sediment starvation of downdrift beaches. Along many shorelines, the return to a tombolo's natural condition has been proposed to promote sediment connectivity and counteract erosion. Nevertheless, the implications of such restorations remain uncertain. In this study, we employ the Delft3D wave-current model to investigate hydrodynamics and sediment dynamics across a tombolo, examining its role as a connector between adjacent beaches. Contrary to expectations, our simulations show only diminutive longshore currents from the updrift beach across the tombolo unless offshore wave heights exceed 8 m. Instead, predominant currents crossing the tombolo originate from offshore of the island, driven by storm-induced water level differences and circulation cells on both sides of the tombolo. The offshore island shelters the downdrift domain, resulting in higher wave energy and dissipation updrift of the tombolo. Further, increasing wave height or wave approach angle not only intensifies water level differences but also relocates circulation cells, enhancing total sediment transport from the updrift beach across the tombolo. However, in general, the deposition of sediment from the updrift side of the domain does not compensate for the sediment loss on the downdrift beach. We conclude that LST across tombolos is limited and occurs only under extreme wave conditions.

Plain Language Summary Longshore transport, the movement of sand and fine gravel along the shoreline driven by waves and tides, plays a crucial role in building and maintaining stable and healthy beaches. Here, we focus on the potential impact of the removal of a road that obstructs water flow and sediment transport across a tombolo. Contrary to our expectations, removal of the road does not result in longshore currents across the tombolo unless the wave heights are very large. Instead, we observe water movement from the offshore of the island's updrift side toward the downdrift beach. This unexpected pattern is attributed to storm-driven water level differences bet side of the island. Additionally, storms generate circulating current patterns on both sides of the island, influencing the direction of water movement. Further investigation reveals that larger waves, particularly those moving more parallel to the beach, amplify the water level difference and alter the location of the rotating currents. Extremely large waves produce longshore currents across the tombolo, which increase the amount of sediment transferred from the updrift to the downdrift domain. However, this addition of sediment from the updrift domain does not fully compensate for sediment loss from the downdrift beach during storms.

1. Introduction

Longshore sediment transport (LST) plays a vital role in shaping the coastal landscape and influencing shoreline evolution. The process allows for sediment redistribution from one location to another, thereby buffering areas undergoing erosion (Giosan et al., 1999; Greer & Madsen, 1978; Shetty & Jayappa, 2020). LST is primarily induced by waves breaking at an oblique angle to the shoreline, resulting in a longshore current flowing within the breaker and surf zones (Hamilton & Ebersole, 2001; Kobayashi et al., 2007). In shoreline systems connected to offshore islands, current patterns may become complex because of circulation cells (Ganju et al., 2011; Klein et al., 2020; Pattiaratchi et al., 2009; da Silva et al., 2021). These cells, characterized by circulation gyres on either side of offshore islands, are formed primarily during storms by large breaking waves interacting with longshore currents along the beach. The circulation cells may shift under varying sea-level rise or storm conditions (Xie

et al., 2024). Consequently, possible sediment bypassing around the islands may be limited, leading to sediment deficiencies and subsequent shoreline erosion along downdrift beaches (King et al., 2021; da Silva et al., 2021). The uneven availability of sediment can also exist in the vicinity of naturally occurring coastal features, such as tombolos and headlands, and human-made structures, such as groins and breakwaters. These features restrict water movement along the shoreline, increasing sediment deposition on the updrift side of the obstacles while reducing sediment availability on the downdrift (Bacon et al., 2007; Cuadrado et al., 2005; Specht et al., 2020). To reestablish the LST and increase sediment availability to downdrift shorelines, an increasing number of coastal managers propose removal of these obstacles (Chi et al., 2023; Nordstrom, 2014). However, questions still exist as to whether such measures would reintroduce effective downdrift sediment supply along these complex shorelines, especially during storms when circulation cells are formed.

The magnitude of LST is influenced by various factors, including wave height, wave angle, nearshore slope, and sediment composition (Chowdhury et al., 2020). For example, Pattiaratchi et al. (1997) reported that even minor increases in wave heights can lead to larger incident wave energy at the shore, potentially resulting in a ten- to hundredfold increase in LST. This is because wave energy and, thus, the resulting radiation stresses and sediment-transporting currents at the shore are proportional to the square of the wave height (Kaliraj et al., 2014). The angles at which waves approach the shoreline are crucial. When waves approach the shore perpendicularly, the resulting wave breaking and energy dissipation predominantly lead to cross-shore sediment transport (Butt et al., 2000). However, waves breaking at an angle to the shoreline create radiation stress, yielding both cross-shore and longshore components. The longshore component of the radiation stress generates longshore currents, which drive the transport of sediment parallel to the shoreline (Chowdhury et al., 2020; Putnam et al., 1949; Vincent et al., 1983). The composition of the bottom sediment plays a crucial role in determining the amount of sediment that can be resuspended. For instance, smaller sediment particles can be transported over greater distances compared to larger ones (Grasso et al., 2011).

Along open coasts, particularly in tropical and subtropical areas, storm-induced coastal sediment redistribution is known to have major geologic and ecological implications (Fagherazzi et al., 2020; FitzGerald et al., 2020; Goman et al., 2005; Hubbard, 1992). However, storm-driven LST in complex settings needs to be further investigated (Yang et al., 2023). Storms generate waves and surges, which can persist for several hours or even days (Villarini et al., 2011). Storm surges allow higher wave energy to reach the shoreline, facilitating nearshore currents that scour beach material, ultimately moving sediment to more sheltered areas (Hequette et al., 2001; Roy et al., 1994; van Wiechen et al., 2023). Storms can also redistribute sediment by resuspending material from deep water and moving it to shallow coastal regions, increasing sedimentation and buffering beaches (Roberts et al., 2013). Along shorelines connected to offshore islands, however, the distribution of wave energy can vary. Offshore islands not only provide shelter, preventing direct wave energy impact on the mainland shoreline, but also induce wave refraction and convergence (Yasso, 1965). This is because the presence of an offshore island shifts the surf zone offshore, thereby lessening the wave energy reaching the shore (Limber et al., 2014). These processes add complexity to nearshore wave energy distribution, particularly during storms. Furthermore, wave energy dissipation gives rise to circulation cells around the offshore island, which have been observed to interact with longshore currents (King et al., 2021; Xie et al., 2024). Previous studies have shown that circulation cells along with tidal currents create a morphological cycle affecting both beach sediment and offshore sandbars (Siegle et al., 2004, 2007). Specifically, in high wave energy systems, circulation cells can redistribute sediment by eroding offshore sandbars, while in low wave energy periods, ebb tidal currents are responsible for creating sandbars through offshore sediment transport. The influence of these circulation cells on LST therefore creates uncertainty in sediment transport rates to downdrift beaches, especially under varying wave energy and storm tide conditions. Further investigation is needed to assess the benefits of altering any updrift structure to promote LST, particularly in complex coastal systems with offshore islands.

In Western Buzzards Bay, Massachusetts, USA, an offshore island, Gooseberry Island, is connected to the mainland by a causeway, part of a headland system along the Westport-Dartmouth shore (Figure 1; Xie et al., 2024). The causeway was initially constructed a century ago on top of a sand and gravel tombolo and has been reinforced and elevated over the decades (Figures 1b and 1c). Currently, the causeway is approximately 10 m wide at the top and 450 m long, with the water depth at the toe being around 2 m. Large boulders (1–2 tons) have been placed along both sides of the causeway to prevent breaching during storms. At the same time, East Beach, the downdrift side of the causeway, has experienced degradation attributed to both sea-level rise and a waning sediment supply (FitzGerald et al., 1987). There are concerns that construction of the causeway diminished

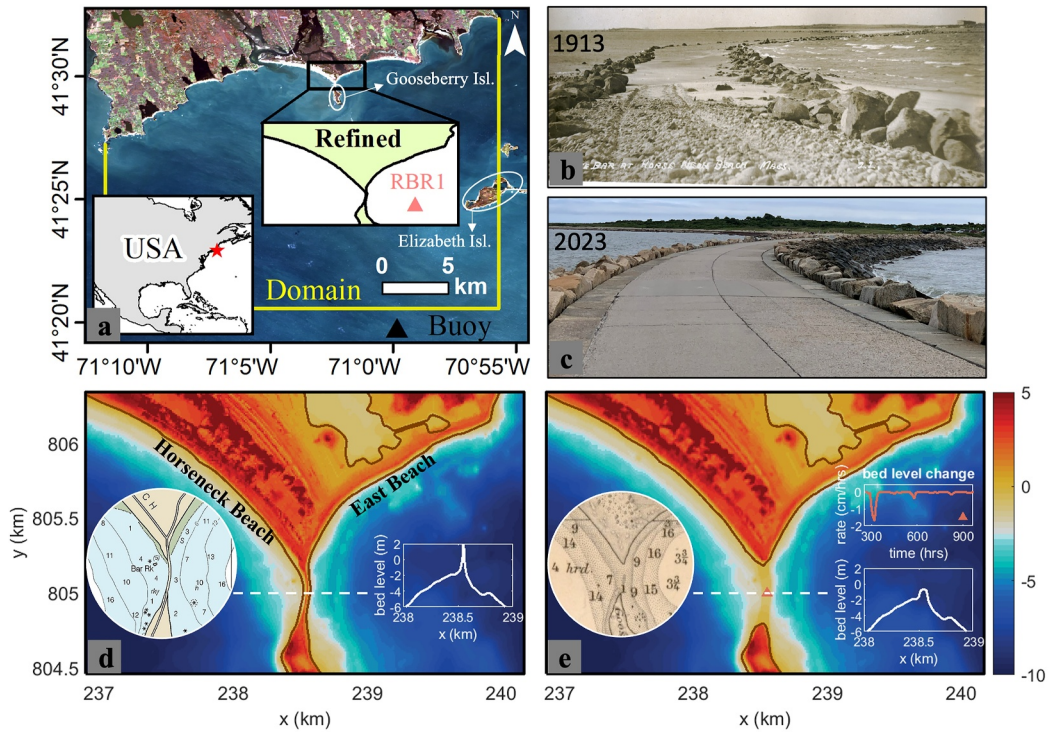

Figure 1. Maps and photos showing the study area (a) Delft3D-FLOW domain is overlayed with a Delft3D-WAVE domain (yellow box). The focus area of this research is modeled with a refined sub-domain (black box) that includes the tombolo where a causeway was constructed at the beginning of the twentieth century. An RBR (Richard Brancker Research) Solo pressure sensor was deployed on the east side of the causeway to measure storm tides and significant wave heights for model validation. The black triangle shows the location of an offshore buoy (Station BUZM3/44085; water depth 21 m) recording wave conditions (wave heights, wave period and wave direction) for model setups. The Elizabeth Islands are located to the southeast of the system. (b) Ground photograph looking southward to Gooseberry Island in 1913 (Clamflats, 2019); Residents placed boulders along the natural tombolo in order to create a path connecting to Gooseberry Island during low tide. (c) Ground photograph looking southward to Gooseberry Island in 2023 (Danghan Xie, August 2023). The causeway has been built up higher than mean high water, potentially obstructing longshore sediment transport. (d) Current bathymetry with a causeway and (e) bathymetry without causeway, which has reached an equilibrium state under non-storm conditions with the constant effects of a 20-cm wave height. Two historical sea charts in panels (d, e) depict the digital elevation model around the tombolo at different times (NOAA, 2024). The inserted line plots in these panels show the elevation across the causeway and tombolo, with modeled rate of bed level change after the bathymetry was altered to represent pre-causeway conditions until equilibrium state was reached, shown in panel (e). The bed level in the two domains is comparable with the sea charts in 2016 (d) and 1892 (e).

sediment transport to East Beach. In response, residents have proposed the removal of the causeway to restore the natural tombolo, which would reestablish sediment connectivity between Horseneck Beach (updrift side) across the tombolo to East Beach (Figure 1d). However, there is limited knowledge concerning potential sediment transport across tombolos, particularly transport associated with storms, which are known to produce circulation cells on both sides of the headland (Xie et al., 2024). This study aims to investigate transport across a natural tombolo, were the causeway not to exist. We address two key questions: (a) Would sediment transport occur across the tombolo? and (b) If so, what factors control the magnitude and direction of currents and sediment transport, including the role of storm surges, significant wave height, and wave direction.

2. Materials and Methods

In this section, we introduced the background information of the study site (Section 2.1), examined the storm characteristics based on 100 historical storm events (Section 2.2), analyzed the sediment data collected from the field, and set up the sediment bed module for the model (Section 2.3). We also determined the model parameter settings and created new bathymetry that included a tombolo (Section 2.4). Furthermore, we validated the models

with measurements recorded during an extratropical storm event (Section 2.5), and designed both idealized and real storm scenarios, creating corresponding boundary conditions (Section 2.6).

2.1. Study Site

The study area is in Western Buzzards Bay along the shores of Westport and South Dartmouth, Massachusetts, USA. This region is part of an indented shoreline that includes an offshore island, Gooseberry Island, connected to the mainland by a manmade causeway (Figures 1a–1c). Along the shoreline, there are two beaches: Horseneck Beach to the west (on the updrift side) and East Beach to the east (on the downdrift side), with Gooseberry Island serving as a natural divider between them (Figure 1d). Due to the sheltering effects of Cape Cod and the Elizabeth Islands, which protect from eastern winds and waves, dominant waves typically originate from south to southwest, with an average nearshore wave height of 0.75 m and a wave period of 6.0 s in 10-m water depth (FitzGerald et al., 1992). Tides within the bay are semidiurnal, with an average tidal range of approximately 1.1 m (FitzGerald et al., 1987; Sankaranarayanan, 2007). Two small rivers on either side of the area contribute negligible amounts of fluvial input, approximately 2 m^3/s (Bent, 1995; FitzGerald et al., 1987). According to the National Oceanic and Atmospheric Administration (NOAA) hurricane database, between 1851 and 2013, a total of 55 hurricanes have impacted the southern New England. One of the most significant hurricanes, Hurricane Bob, produced a storm surge of approximately 2.8 m and peak storm waves exceeding 8 m (Sun et al., 2013). Such extreme storm events resulted in significant sediment transport and shoreline change in the coastal system (Cheung et al., 2007). In addition to hurricanes, coastal flooding and damage in this region are also frequently caused by extratropical cyclones (also known as Nor'easters or winter storms; Zhang et al., 2020).

2.2. Storm Characteristics

To characterize storm conditions in this region, we analyzed storm surge, peak storm wave height, and storm wave direction from 1938 to 2012 using data obtained from the North Atlantic Coast Comprehensive Study (NACCS) Coastal Hazards System at the buoy location (BUZM3, black triangle in Figure 1a; Cialone et al., 2015). This database includes 100 historical storms, predominantly from extratropical cyclones. We identified the frequency of storm characteristics by calculating density histograms and the probability density function (Kernel Density Estimate) for each storm, following the methodology outlined by Bai et al. (2020). A higher probability density value indicates that storm characteristics (e.g., storm surges, peak waves, or wave direction) of this magnitude have historically been more frequent.

For our study site, the most prevalent storm surge is approximately 0.65 m, and the most frequently observed peak wave height during storms is approximately 4 m (Figures 2a and 2b). The maximum storm wave height in this area can surpass 10 m, but such occurrence is highly infrequent (Figure 2b). The dominant wave direction is 185°,

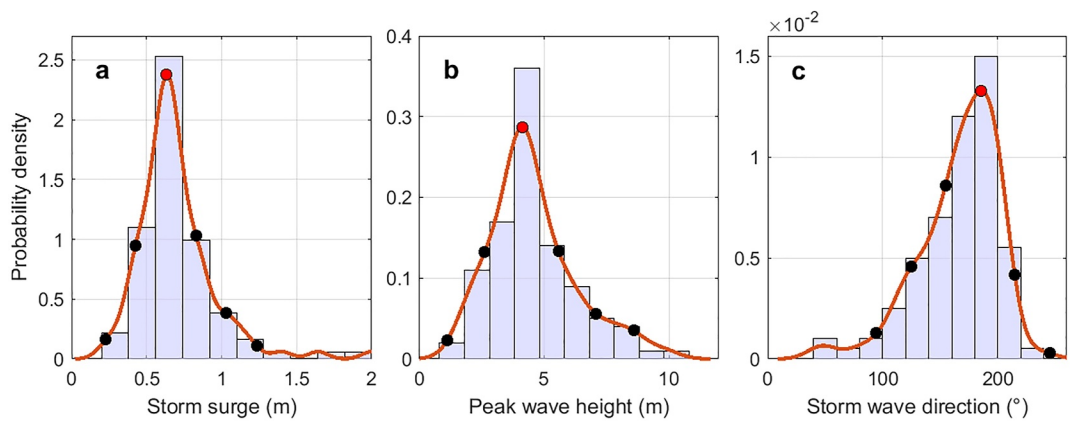

Figure 2. Normalized histogram and kernel density estimate (KDE) curve of historical storm characteristics extracted from the NACCS Coastal Hazards System (Point No. 09088). The storm characteristics examined here include (a) storm surge, (b) peak storm wave heights and (c) storm wave direction. The KDE curve provides a smooth estimate of the underlying probability density function of the data generated using a Gaussian kernel function. Wave direction in panel (c) is based on Nautical convention with 0° indicating waves coming from the north and 90° indicating waves traveling from the east.

Table 1
Model Scenarios for Synthetic and Historical Storms

No.	Group	Storm surge (m)	Storm wave height (m)	Storm wave direction (°)	Note
1	Impacts of storm surge	0.25	**4**	**185**	-
2		0.45			-
3		**0.65**			REF
4		0.85			-
5		1.05			-
6		1.25			Surge +
7	Impacts of storm wave height	**0.65**	1	**185**	-
8			2.5		-
Same as No. 3			**4**		REF
9			5.5		(extreme storm)
10			7		(extreme storm)
11			8.5		Wave + (extreme storm)
12	Impacts of storm wave direction	**0.65**	**4**	95	-
13				125	-
14				155	-
Same as No. 3				**185**	REF
15				215	-
16				245	-
17	Historical storms	0.45	5.3	193	2022- Extratropical Storm Elliott (extreme storm)
18		0.71	8.7	191	2011-Hurricane Irene (extreme storm)
19		2.77	8.8	176	1991-Hurricane Bob (extreme storm)

Note. (1) Reference idealized storm is indicated in bold; (2) Storm surge, wave heights, and wave direction vary over time in three historical storms, with the values during peak wave heights indicated in 17–19.

indicating prevailing waves coming from the south (Figure 2c). The storm characteristics provide a reference for our numerical model scenario setups. In the following text, the reference scenario is abbreviated as REF. The storm surge and wave input for the model runs are derived from the frequency distributions (black and red dots in Figure 2) covering different probability densities of each parameter (see Table 1 introduced in Section 2.6, where the bold font indicates the highest probability).

2.3. Sediment Sampling and Sediment Profile Compilation

We collected a total of 200 sediment samples, covering areas from deep water (~15-m water depth) to the beach system (see circles in Figure 3a). In agreement with a previous study by FitzGerald et al. (1992), we found that almost 85% of the Western Buzzards Bay sediment samples contained sand, with only 8% being gravel. The samples were sieved to determine the median grain size (d_{50}, Figures 3c–3f). The average d_{50} across the samples was approximately 230 μm, whereas the gravel ranged from 5,000 to 35,000 μm, with an average size of nearly 20,000 μm (Figures 3e and 3f). Thus, our numerical model considered these two grain size classes. The median grain size for sand was set to 230 μm, and for gravel, it was set to 20,000 μm.

In addition, sediment deposits in the area display upward fining, with coarser sediment underlying finer grained sand (FitzGerald et al., 1992). We therefore set up the bed module by combining two sediment layers for the sediment profiles in both large and refined model domains (Figure 3b). Sediment classes of layer 1 were determined based on the sediment texture map provided by USGS (Foster, 2014), which exhibits a similar distribution of sediment to the samples collected from the field (Figure 3a). As sand is the dominant sediment class in the study area, we assumed that the missing data region in the bottom left of the domain consists mainly of sand

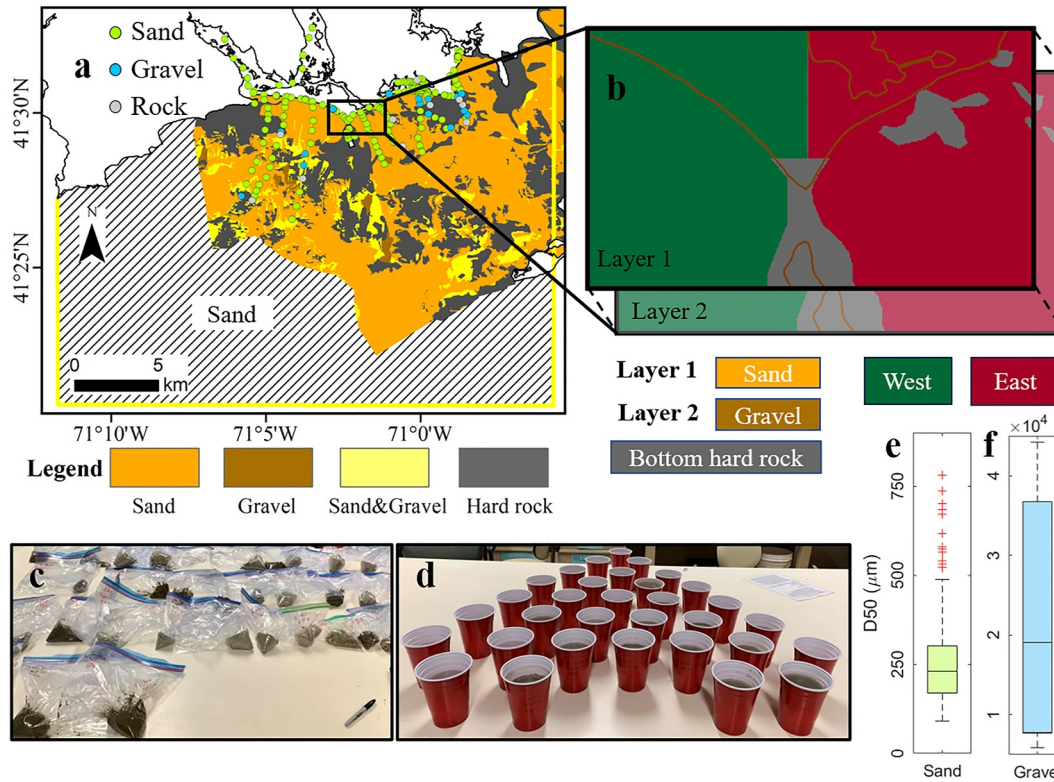

Figure 3. Domain sediment profile setups. (a) Sediment texture map and field points collected for sediment sampling. The sediment texture map indicates the spatial sediment types within Western Buzzards Bay, which mainly contains sand and gravel overlaying hard rocks (Foster, 2014). (b) Two-layer bed module in the refined model. Sediments in the west and east domains are configured separately to trace the sediment movement between the west and east regions. (c) Sediment samples collected from the field. (d) Pre-cleaning of sediment before drying. Median grain size (d_{50}) of sand (e) and gravel (f).

(see the hatched region of Figure 3a). In non-hard rock regions, a second layer was introduced under layer 1 (Figure 3b). Layer 2 was assigned as gravel to replicate the pattern of upward fining (FitzGerald et al., 1992). The thickness of each sediment layer was set to 50 cm. To identify the sources of sediment and determine the amount of sediment transported across the tombolo, sediment in the west and east domains were set up separately (Figure 3b). Transport of sand and gravel in the model used the Van Rijn transport equations, with suspended-load transport and bed-load transport calculated separately (van Rijn et al., 2004). Transport of suspended sediment was determined using the advection-diffusion equation. In this study, we refer to the area updrift of the causeway as the west domain and the area downdrift of the causeway as the east domain (Figure 3b).

2.4. Model Setup

Following our previous research investigating the formation of circulation cells in this area (Xie et al., 2024), we further explored the hydrodynamics and sediment transport around the tombolo using the spatially resolved and process-based model Delft3D (Lesser et al., 2004). We focus on wave-current interactions, including the impacts of flow on waves (via set-up, current refraction, and enhanced bottom friction) as well as the effects of waves on currents (via forcing and enhanced bed shear stress). We employed an online-coupled model between Delft3D-WAVE and Delft3D-FLOW. Delft3D-WAVE models wave propagation and wave energy dissipation based on the third-generation spectral wave model SWAN (Simulating WAves Nearshore; Booij et al., 1999), while Delft3D-FLOW simulates hydrodynamics and sediment transport by solving the depth-averaged shallow water equations. To better capture flow and sediment dynamics around the tombolo while improving computational efficiency, the domain was divided into two parts. A locally refined model domain was established around the tombolo (indicated by the black box in Figure 1a), and a larger model domain covered the rest of Western Buzzards Bay (indicated by the yellow box in Figure 1a) using the domain decomposition technique (Deltares, 2014; Zhu & Wiberg, 2022). The refined model does not extend to cover the full Gooseberry Island and its

neighboring area because: (a) our main focus centers on the tombolo region, (b) computation efficiency is significantly enhanced with a smaller region, and (c) the west sediment moving onshore to East Beach through the offshore of Gooseberry Island is minimal compared to the major sediment movement across the tombolo (Figure S1 in Supporting Information S1).

The refined model domain around the tombolo contained 326 × 190 (X × Y direction) rectangular grid cells with a uniform spatial resolution of 10 m by 10 m. The large model domain consisted of 469 × 389 rectangular grid cells. Near the shoreline and island, the grid resolution was 40 m by 40 m, gradually extending to 40 m by 80 m at the southern seaward and northern landward boundaries in the cross-shore direction. The domain decomposition technique enabled parallel computation between the refined model and large model domains, with hydrodynamic information and sediment transport exchanged along the shared boundaries at each time step (Figure 1a). The initial bathymetry for the two domains was interpolated from a high-resolution digital elevation model (DEM) developed by NOAA for the USA coast (CIRES, 2014). The DEM data have a horizontal resolution ranging from 1 m to 30 m and a vertical resolution smaller than 1 m. To assess potential changes in hydrodynamics and sediment transport after the removal of the causeway, we developed new bathymetry by lowering the elevation of the causeway to the mean water level. This was followed by a long-term simulation with idealized tides and waves until the bed level change at the tombolo remained negligible (see the inserts in Figures 1d and 1e). During this simulation, the tidal range was set to 1 m and the wave height was set to 0.2 m. Compared to the historical sea chart from the year 1892, where the elevation around the tombolo was approximately 1 foot (=0.3 m) below the mean low water level (around 0.9 m below mean water level), our new bathymetry depicts a tombolo elevation of 1 m below the mean water level, nearly identical to the data shown in the sea chart (Figure 1e). Thus, we assume that the new bathymetry successfully reproduced the naturally formed tombolo. The tombolo is set to be non-erodible during simulations, enabling us to focus on the sediment transport between updrift and downdrift systems without interference from sediment erosion from the tombolo.

2.5. Model Validation

Validation encompassed both large and refined models where the causeway is present. In a previous study, validation of the large model involved comparison against two ADCPs measuring data and 43 validation points extracted from the NACCS Coastal Hazards System (Xie et al., 2024). To validate the refined model, high frequency water level and wave records were obtained using an RBR-Solo pressure sensor (RBR1) installed on the east side of the causeway from July–November 2022 (Figure 1a). RBR1 successfully captured water level and wave height during the winter storm of November 2022. To evaluate our refined model performance, we calculated the model skill index using the validation approach proposed by Willmott (1981). The skill index is defined as:

$$\text{Skill} = 1 - \frac{\sum |X_D - X_S|^2}{\sum \left(|X_D - \overline{X_S}| + |X_S - \overline{X_S}| \right)^2} \quad (1)$$

where X_D is the refined Delft3D model output and X_S is the measured data from RBR1, both of which are applied herein at hourly intervals. $\overline{X_S}$ is the temporal average of the data points from measurements. The skill index ranges between 0 and 1, where 1 indicates a perfect match between the model output and reference samples, and 0 indicates a complete failure to capture the expected behavior. Previous research suggests that a skill index higher than 0.7 to 0.8 represents a reasonable prediction, particularly for wave heights (Warner et al., 2005; Xie et al., 2024; Zhu & Wiberg, 2022). Results indicate that our local refined model could effectively capture changes in water level and wave height during storms given their high skill index (Figure 4).

2.6. Model Scenarios and Boundary Conditions

To understand the impacts of storm characteristics on hydrodynamics and sediment transport across the tombolo, we designed three groups of experiments by setting up a series of idealized storms (Table 1). A reference storm condition (indicated by the bold number in Table 1) was established using the most probable values of the storm characteristics (highlighted by the red dots in Figure 2). Subsequently, the impact of storm surge, storm waves, and storm wave direction were individually examined by varying the parameters according to the probability distributions of Figure 2. The probability occurrence of these idealized storm scenarios varies, with a higher

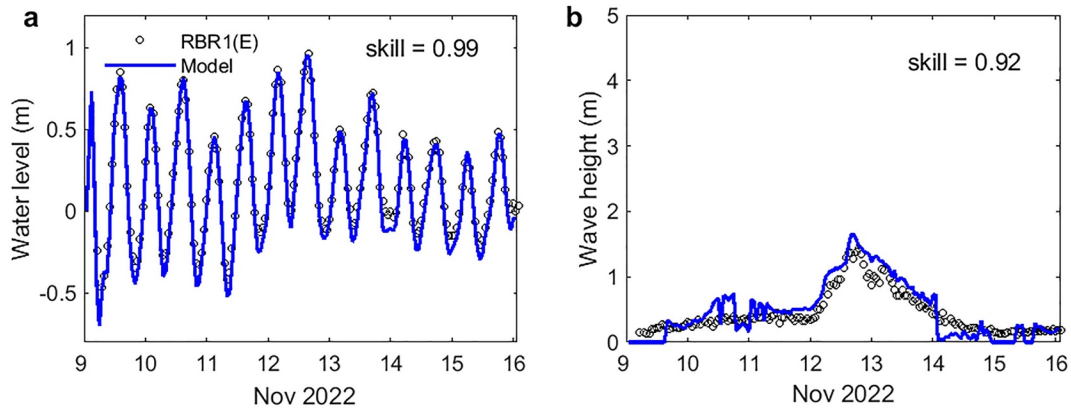

Figure 4. Comparison between Delft3D refined model output and observation data at the site of RBR1 during the winter storm of November 2022: (a) water level and (b) wave height.

likelihood of occurrence for the reference scenario (Figure S2 in Supporting Information S1). However, it is important to note that the combinations with minimum or maximum values of the examined parameter within each group rarely occur in nature. For example, a 4-m storm wave height generally appears with a storm surge ranging between 0.40 and 1.12 m, whereas a 1.25-m storm surge might be slightly beyond this range (Figure S3 in Supporting Information S1). In these idealized storms, tidal signals at the southern boundary were designed by overlaying a 0.5-m S2 tidal signal with the corresponding storm surges (Figure 5a and Figure S4 in Supporting Information S1). The storm surge period is set to 24 hr based on the probability density distribution of historical storm surge durations (Figure S4c in Supporting Information S1). Following previous studies, a cosine-shaped curve is applied to mimic the changing trend of the storm surge during the 24 hr (Dullaart et al., 2023; Ma et al., 2024; Zhou et al., 2022). Peak surge conditions were timed to coincide with high tide to maximize the storm

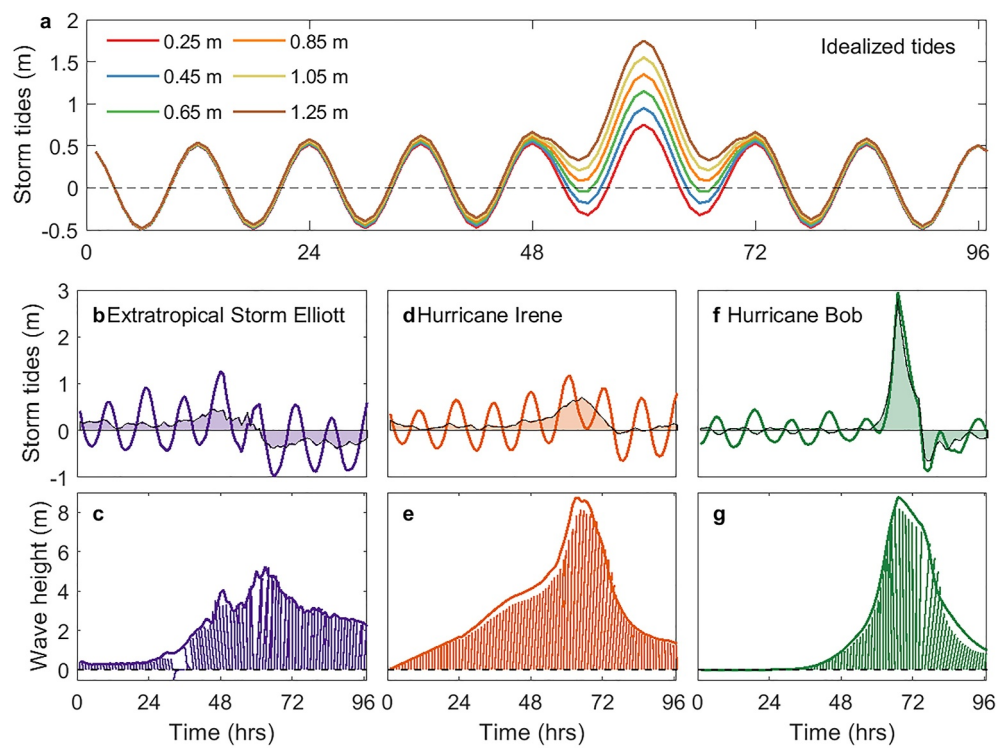

Figure 5. Boundary conditions for the model runs. Idealized storm tides (a), and three historical storms including Extratropical Storm Elliott (b, c), Hurricane Irene (d, e) and Hurricane Bob (f, g). Storm surges are indicated as shaded areas in panels (b, d, f). Line vectors in panels (c, e, g) point to the direction where the waves are propagating toward.

Table 2
Joint Probability of the Examined Model Scenarios

Scenario name	Storm surge (m) [bin range]	Wave height (m) [bin range]	Wave direction (°) [bin range]	Number of storms	Joint probability
REF	0.65 [0.56–0.74]	4 [3.8–4.8]	185 [180–200]	8	8%
Surge +	1.25 [>0.74]	4 [3.8–4.8]	185 [180–200]	1	1%
SW wave	0.65 [0.56–0.74]	4 [3.8–4.8]	215 [200–220]	3	3%
Wave +	0.65 [0.56–0.74]	8.5 [>6.8]	185 [180–200]	2	2%
Elliott	0.45 [0.38–0.56]	5.3 [4.8–5.8]	193 [180–200]	2	2%
Irene	0.71 [0.56–0.74]	8.7 [>6.8]	191 [180–200]	2	2%
Bob	2.77 [>0.74]	8.8 [>6.8]	176 [160–180]	2	2%

tides. The wave height, wave period, and wave direction are kept constant throughout the simulation at the boundary (Figure S5a in Supporting Information S1). Wave periods for these idealized storm scenarios are determined using a previously established empirical relationship between wave period (T_p) and wave height (H_s), given by $T_p \approx 5.3\sqrt{H_s}$ (Mangor et al., 2017). Here, a storm surge is defined as the abnormal elevation of water caused by a storm, exceeding the expected astronomical tide, and storm tides refer to the water level during a storm resulting from the combination of storm surge and astronomical tide.

In addition to the idealized storm scenarios, we also incorporated three historical storm events: Extratropical Storm Elliott (2022), Hurricane Irene (2017), and Hurricane Bob (1991) (Figures 5b–5g). Water level information during Extratropical Storm Elliott and Hurricane Irene was based on the tidal gauge at Newport (Station No.: 8452660) operated by NOAA and located 20 km away from the southern boundary (NOAA, 2023). Wave heights, wave periods, and wave direction were obtained from the offshore buoy station (Figure 1a) maintained by the National Data Buoy Center (NDBC, 2023). The boundary conditions for Hurricane Bob, including storm tides and waves, were obtained from the Massachusetts Coastal Flood Risk Modeling developed by Woods Hole Group (https://www.woodsholegroup.com/). Waves originated from the south for all the historic storms (Figures 5c–5e and 5g). The storm surge for Extratropical Storm Elliott was approximately 0.4 m, with a peak wave height of 5 m (Figures 5b and 5c). The storm surge for Hurricane Irene nearly doubled that of Elliott, reaching 0.7 m, with a peak wave height of around 8.7 m (Figures 5d and 5e). This wave height was similar to that observed during Hurricane Bob (Figure 5g). However, Hurricane Bob generated a substantial storm surge of approximately 2.8 m (Figure 5f) as simulated by the Coastal Flood Risk Modeling. During these historical storm events, wave periods varied with each storm and changed over time (Figure S5b in Supporting Information S1).

In our analysis, we modeled four idealized storms (including REF, Surge +, SW wave, and Wave +) and three historical storms (including Elliott, Irene, and Bob) (Table 1). The frequency probability of these storms is provided in Table 2. Joint probability is based on the proportion of storms having similar storm characteristics. Moreover, we established a relationship between peak storm wave height and annual exceedance probability to assess the severity of wave conditions examined in this study (Figure S6 in Supporting Information S1). Here, an extreme storm event is defined as one generating peak wave heights with a return period exceeding 1 year. Consequently, scenarios involving extreme wave climates refer to: (a) idealized storms with wave heights greater than the reference scenario, and (b) the three historical storms (Table 1).

The idealized storm simulations maintain constant wave conditions for the entire 96-hr period. In contrast, although the historical storms were also simulated for 96 hr, the duration of their peak waves varied and was notably shorter than the constant wave duration in the idealized storms (Figure 5). To mitigate instability arising from the transition from initial conditions to the dynamic boundary conditions in the hydrodynamic simulation, each scenario included a 24-hr spin-up period at the beginning, during which the effect of the sediment fluxes on the available bottom sediments were not taken into account (Deltares, 2014). In addition to the storm tides and storm wave boundary conditions, the other open boundaries in the large model domain included: (a) two upstream river discharge boundaries (set to 2 m^3/s) based on statistics of annual river discharge measurements (Bent, 1995; FitzGerald et al., 1987; Xie et al., 2024), and (b) two Neumann boundary conditions on the western and eastern boundaries.

3. Results

Results consist of two sections: Section 3.1 presents the spatial distribution of coastal hydrodynamic conditions around the tombolo during different idealized storms, and Section 3.2 quantifies the amount of sediment transported across the tombolo for different storms.

3.1. Impacts of Storms on the Hydrodynamic Conditions Around the Tombolo

Causeway removal allows currents to transport sediment across the tombolo during storms, in this case from the west to the east domain, because the predominant waves come from the south to southwest, with higher wave energy observed on the west. However, the currents connecting the two domains are dominated by offshore circulation cells driven by waves breaking along either side of the island and subsequently connecting with longshore currents along the beach (Figures 6 and 7).

The reference idealized storm generates a 4-m wave height at the wave boundary, propagating northward with a storm surge reaching up to 0.65 m. Wave vectors gradually refract toward Gooseberry Island (Figure 6a), and due to the protection of the island, wave heights at the tombolo area are smaller than the wave heights on the nearby beach (Figure 6b). Furthermore, wave heights on the west domain are higher than those on the east domain (Figures 6a and 6b). This is because the presence of the offshore Elizabeth Islands and Gooseberry Island shelters the region (see Figure 1a), thereby reducing wave energy in the east side of the system (Figure S7 in Supporting Information S1). The larger waves in the western area dissipate in the surf zone (Figures 6c and 6d), leading to a rise in local water level (wave set-up) and creating a water level differential on the two sides of the tombolo (Figures 6e and 6f). This water level difference is expected to generate horizontal currents flowing from the west domain to the east domain. However, wave-generated currents around Gooseberry Island form two circulation cells, one counterclockwise and one clockwise, symmetrically distributed on the west and east sides of the island (Figure 7a). These circulation cells interact with the current driven by the water level differential, drawing the flow along the west side of the island and across to the beach on the east side (Figure 7b).

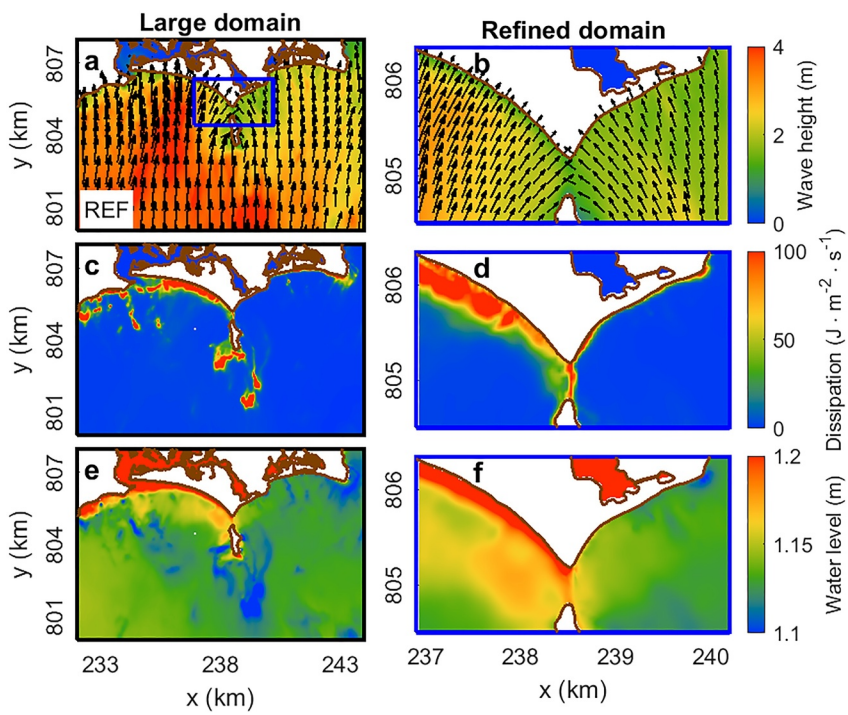

Figure 6. Hydrodynamic conditions around the tombolo in the reference scenario (REF) where waves come from the south. Wave propagation map (a, b), wave energy dissipation rate (c, d) and water level (e, f). Results are shown in two different domain sizes: large domain (a, c, e) and refined domain (b, d, f). The large domain extends beyond the island area, while the refined domain specifically focuses on the area around the tombolo.

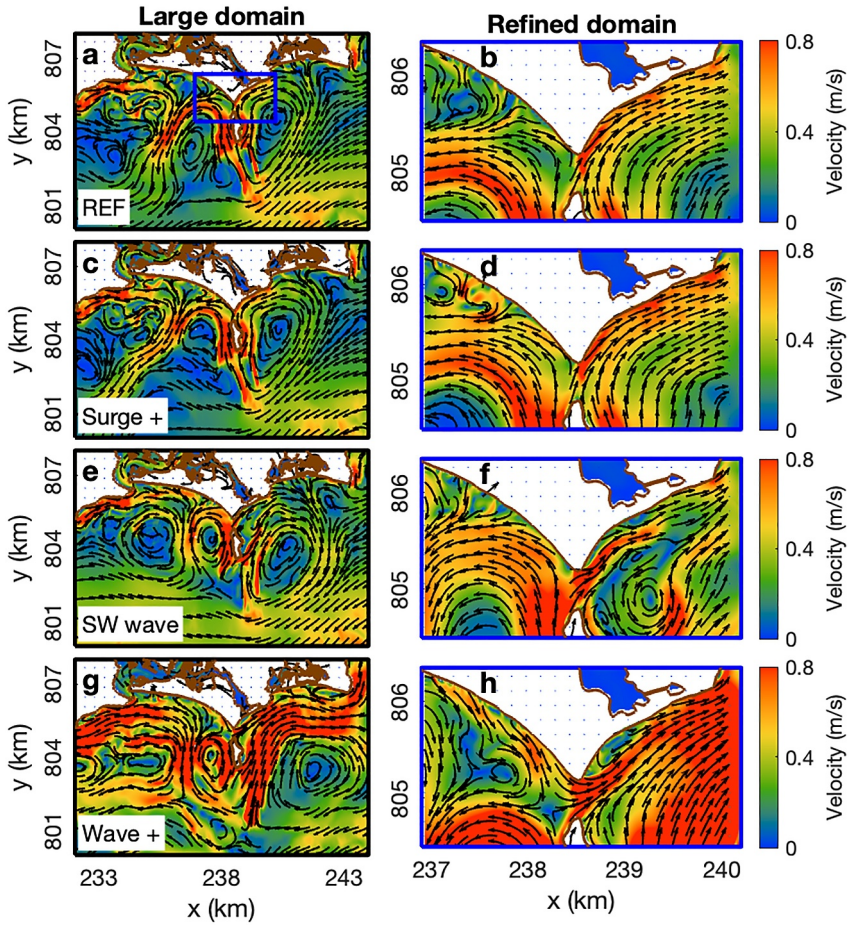

Figure 7. Flow velocity fields with the formation of circulation cells on the two sides of the island under different idealized storm scenarios. Here, Surge + refers to the scenario with 1.25 m storm surge (c, d); SW wave refers to the scenario where waves come from southwest (215°; e, f). Wave + refers to the scenario with 8.5 m wave heights (g, h).

The position, magnitude, and size of the circulation cells vary with storm surge, wave height, and wave direction, which in turn influence currents across the tombolo (Figure 7). A higher storm surge shifts the two cells landward, resulting in an increase in velocity on both sides of the island (Figure 7d). Differing from the reference scenario, which creates two symmetric circulation cells (Figure 7a), the incoming waves from the southwest produce asymmetric circulation cells (Figure 7e). Specifically, the circulation cell in the west domain moves closer to the shoreline, while the east cell migrates further eastward and seaward, causing the strong flows along East Beach to shift slightly offshore (Figure 7f). Meanwhile, the landward migration of the west circulation cell not only augments nearshore currents on Horseneck Beach but also accelerates flow across the tombolo (Figure 7f). In the large wave scenarios, although the two circulation cells have migrated seaward, their magnitude and size are enhanced, particularly the eastern cell (Figure 7g). Importantly, large waves produce eastward flow along the west beach toward the tombolo, potentially creating a new sediment transport path from Horseneck Beach to East Beach (Figure 7h).

3.2. Sediment Transport Across the Tombolo

The removal of the causeway potentially enables sediment transport across the tombolo during storms. The predominant sediment flux originates from the west domain and moves toward the east domain, driven by either larger waves or waves approaching from the southwest (Figure 8).

In the reference scenario, the peak sediment flux across the tombolo from west to east is nearly three times larger than the peak flux from east to west. Sediment transport from the west to the east domain reaches a maximum of 0.15 kg/m/s, while the flux in the opposite direction remains low at 0.05 kg/m/s (see "REF" in Figure 8a). The

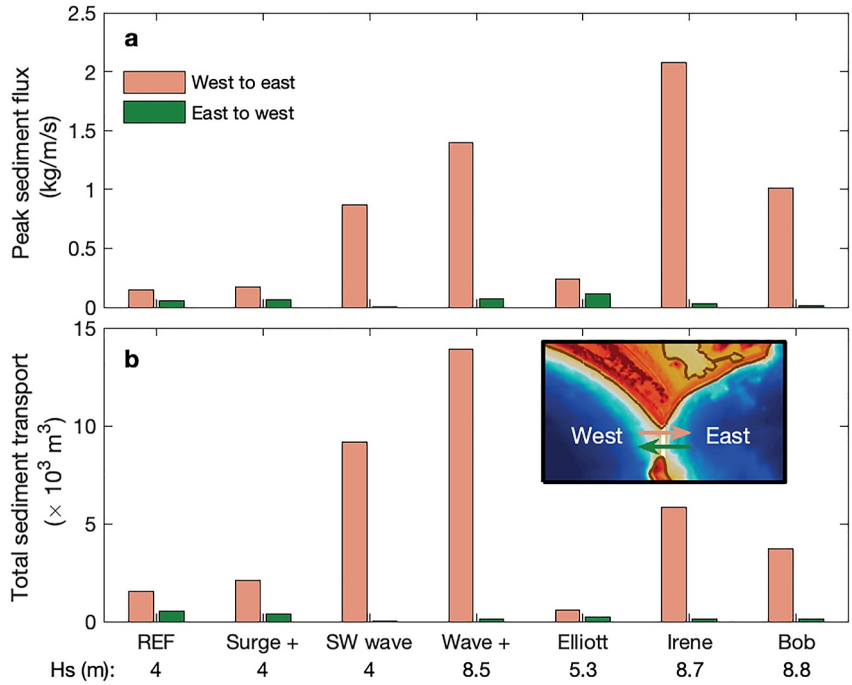

Figure 8. Peak sediment flux (a) and total cumulative sediment transport across the tombolo (b). Sediment transport across the tombolo is quantified along the transect indicated in panel (b). The magnitude of sediment transport is calculated as the sum of the suspended load and bed load. Three historical storms, including Extratropical Storm Elliott, Hurricane Irene and Hurricane Bob are also examined. The corresponding peak wave heights (Hs) are indicated below each scenario.

difference in sediment flux results in a prevailing west-to-east sediment transport under the most frequent storm conditions. Storm surge appears to have a limited role in sediment transport (see "Surge +" in Figure 8a), while significant changes are observed when waves come from the southwest or under more intense wave conditions (see "SW wave" and "Wave +" in Figure 8a). For instance, with southwest waves or with double wave height (8.5 m), the sediment transport from west to east increases by 5 and 8 times, respectively (i.e., 0.87 kg/m/s in "SW wave" and 1.39 kg/m/s in "Wave +"). Conversely, in both scenarios, the sediment flux from the east domain to the west domain is nearly negligible, approximately 0.003 kg/m/s in "SW wave" and 0.07 kg/m/s in "Wave +."

In addition to the idealized scenarios, we also examine sediment transport during three historical storm events: Extratropical Storm Elliott, Hurricane Irene, and Hurricane Bob (Figure 8a). Elliott displays a slightly higher sediment flux from west to east (0.24 kg/m/s) compared to the reference scenario, likely attributed to its 1 m higher significant wave height (see "Elliott" in Figure 8a). On the other hand, Hurricanes Irene and Bob, which exhibit nearly identical significant wave heights of approximately 8.5 m, demonstrate a substantial increase in sediment transport from west to east, reaching 2.08 kg/m/s during Hurricane Irene and 1.01 kg/m/s during Hurricane Bob. The east-to-west sediment flux during both storms is significantly lower, below 0.05 kg/m/s.

In the idealized storm settings (i.e., constant storm wave conditions), total sediment transport is a function of the peak sediment flux (see "REF," "Surge +," "SW wave" and "Wave +" in Figure 8). In the reference scenario, cumulative sediment transport from the west domain to the east domain is around 1,500 m^3 over a 72-hr storm period, while the sediment transport from the east domain to the west domain is approximately 500 m^3 ("REF" in Figure 8b). The storm surge has a limited impact on the total sediment transport ("Surge +" in Figure 8b). Furthermore, waves from the southwest or intense storm conditions (4 and 8.5 m significant wave height) cause a larger total sediment transport compared to the reference scenario, transporting cumulative sediment volumes of 9,000 and 14,000 m^3, respectively (Figure 8b).

In addition to the magnitude of wave height and the angle of wave incidence, sediment transport across the tombolo is also affected by the duration of the storm (Figure 8b). Extratropical Storm Elliott, despite having peak waves 1 m larger than the reference storm, transports only about half the total sediment, amounting to 580 m^3 ("Elliott" in Figure 8b). Hurricanes Irene and Bob produce slightly higher peak wave heights than "Wave +";

however, due to the shorter duration of large wave conditions (Figure 5), the total sediment flux from the west to the east domain is lower (5,800 m^3 during Hurricane Irene and 3,600 m^3 during Hurricane Bob). All three storms produce negligible sediment transport from the east to the west of the island (Figure 8b).

4. Discussion

Our numerical scenarios reveal that storms create water level differences in both sides of the tombolo as well as coastal circulation cells. These cells can vary in position, magnitude, and size during different storm events. The interaction between circulation cells and nearshore hydrodynamics plays a significant role in sediment transport across the tombolo.

Our scenarios include both idealized and real storm events, with variations in storm surge, peak storm wave height, and wave direction. Below, we discuss how water level differences control the horizontal velocity across the tombolo (Section 4.1.1) and how circulation cells influence the northward velocity component (Section 4.1.2). Additionally, we explore the impact of horizontal and vertical sediment grain size distribution on sediment transport across the tombolo (Section 4.2) and trace the sediment sink on the east domain, when the sediment source originates from the west domain (Section 4.3). Finally, we address other relevant processes influencing sediment transport across the tombolo and propose potential future research directions related to the tombolo systems (Section 4.4).

4.1. Impacts of Storms on the Flow Velocity Across the Tombolo

Our model simulations show that longshore currents do not cross the tombolo for moderate to low wave energies, such as during the reference and southwest-wave storm conditions (Figure 7). Such current patterns only occur during large storms (Figure 7h). We also show that velocity across the tombolo does not correlate with longshore currents (Figure S8 in Supporting Information S1). This is different from longshore currents along a straight shoreline that move parallel to the beach (Kobayashi et al., 2007; Longuet-Higgins, 1970). Instead, our model results indicate that the dominant current moves across the tombolo from the west of the island onto East Beach (Figures 7b–7d and 7f). This is likely due to (a) the water level difference between the two sides of the tombolo (Figures 6f) and (b) the circulation cells generated on either side offshore of the island, which modulate the currents across the tombolo (Figures 7a–7c and 7e and 7g). Below, we explain the factors controlling the current patterns across the tombolo in more detail.

4.1.1. Storm-Driven Water Level Differences Amplify Horizontal Velocity Across the Tombolo

In addition to storm surges, wave set-up plays a crucial role in elevating water levels during storms (Lerma et al., 2017; Wang et al., 2020). The magnitude of wave set-up in coastal areas is determined by wave energy dissipation, which leads to a radiation stress gradient transferring momentum from the wave to the water column (Hoque et al., 2019; Svendsen, 1984; Woodworth et al., 2019). In our system, variations in wave energy dissipation between the west and east domains result in differences in wave set-up, thereby generating differential water elevations on either side of the tombolo (Figures 6c–6f). This is because offshore islands, such as the Elizabeth and Gooseberry Islands, interrupt the propagation of waves toward the eastern shoreline, thereby sheltering them (Figure S7 in Supporting Information S1) and diminishing wave energy dissipation in the east domain (Figures 6c and 6d). Difference in wave set-up induced by wave height variations has also been reported in a previous field observation and modeling study by Lavaud et al. (2022).

We explore the effects of various storm parameters, including storm surge, peak wave height, and wave direction, on the water level difference between the west and east domains. Subsequently, we examine the potential correlation between horizontal velocity across the tombolo and water level difference (Figure 9). In the idealized storm scenarios, wave height controls the water level gradient across the tombolo (Figure 9b) rather than the storm surge (Figure 9a). Wave direction, while playing a secondary role, amplifies the water level differences, particularly when waves originate from the southwest (Figure 9c). This is important because a significant correlation exists between water level difference and the horizontal flow across the tombolo (Figure 9d).

The relationship between the water level gradient and flow speeds across the tombolo is further supported by hourly data points observed during the three historical storm scenarios (Figure 10a). Modulation of flow velocity, influenced by water level differences driven by wave set-up, aligns with observations from previous studies

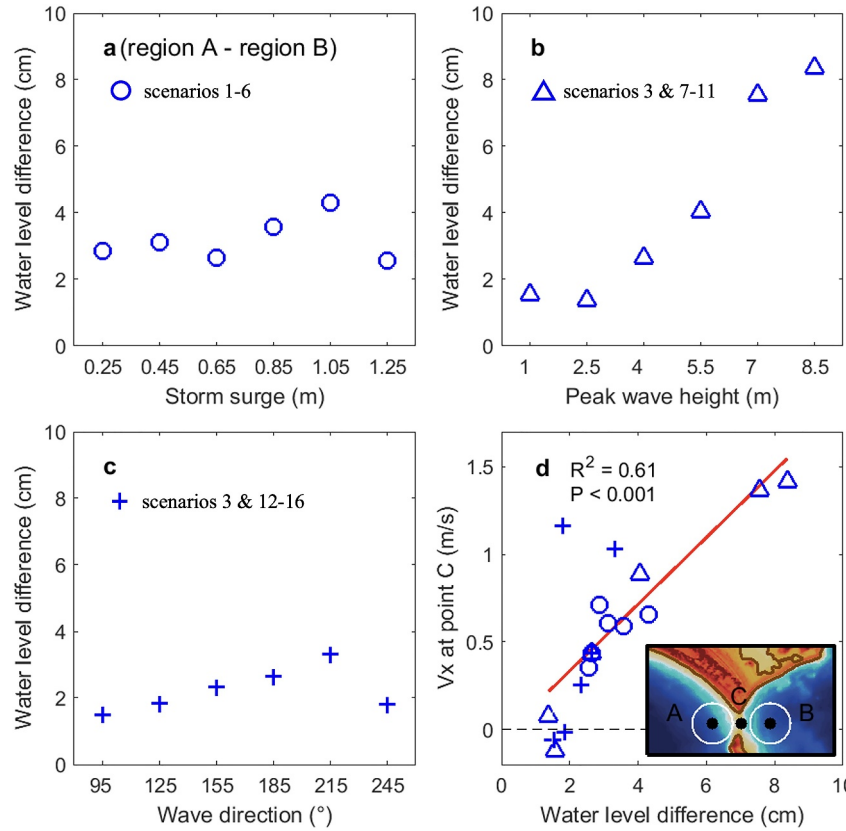

Figure 9. Relationship between the storm-driven water level difference and the horizontal velocity across the tombolo. Variations in water level difference between the west and east domains are depicted in relation to storm parameters, including storm surge (a), peak wave height (b), and wave direction (c). Panel (d) illustrates the correlation between horizontal velocity across the tombolo and water level difference. The coefficient of determination (R^2) and p value for the linear regression are annotated. As indicated in the inserted map in panel (d), the water level difference is calculated based on the 90th percentile of the water level in regions of A and B represented by the white circle around the black points, and the horizontal velocity at the tombolo is extracted from point C. Data points represent conditions at the peak of the storm surge.

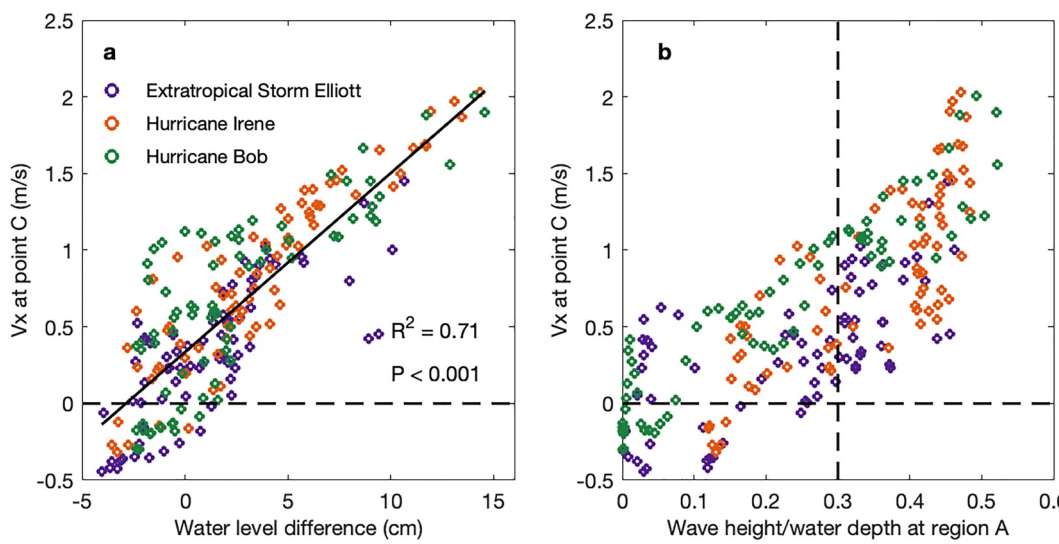

Figure 10. Relationship between horizontal velocity across the tombolo and water level difference (a), and the ratio of wave height to water depth (b). Data points are based on hourly data over the entire storm period. The vertical dashed line in panel (b) indicates a threshold above which the horizontal velocity across the tombolo is always positive.

(Dodet et al., 2019; Idier et al., 2019; Woodworth et al., 2019). Moreover, analysis reveals that flow across the tombolo is influenced by the ratio of wave height to water depth at region A (Figure 10b). Specifically, when this ratio exceeds 0.3, the velocity remains positive, indicating that currents move from the west domain to the east domain.

4.1.2. Storm-Driven Circulation Cells Amplify the Northward Velocity Component Across the Tombolo

A significant finding in our study is the emergence of two circulation cells west and east of Gooseberry Island during storms (Figure 7). Formation of circulation cells has also been observed in previous studies of similar sandy bay-headland systems, disturbing local current patterns (George et al., 2019; Klein et al., 2020; McCarroll et al., 2018). The existence of these cells is linked to waves breaking around the offshore island or headland, where currents are intensified (Vieira da Silva et al., 2018). This process can be seen in our model results, where wave dissipation around Gooseberry Island accelerates local currents (Figures 6c and 6d and 7). These circulation cells induce counterclockwise rotating currents in the west domain and clockwise rotation in the east (Figure 7). As a result, currents traversing the tombolo, driven by water level differences, interact with the circulation cells, flowing cross-shore from the west side of Gooseberry Island to East Beach, rather than moving parallel to the mainland shoreline, from the beach across the tombolo (Figures 7b–7d and 7f and 7h).

Our findings also indicate that the position, magnitude, and size of the two circulation cells are affected by storm characteristics. For example, an increase in storm surge accelerates northward velocity along the west side of Gooseberry Island (Figure 11a), which can be attributed to the landward shift of the circulation cells. This phenomenon is aligned with a previous study that presented a landward shift of circulation cells driven by sea-level rise (Xie et al., 2024). Higher water levels allow waves to propagate further onshore and move the primary

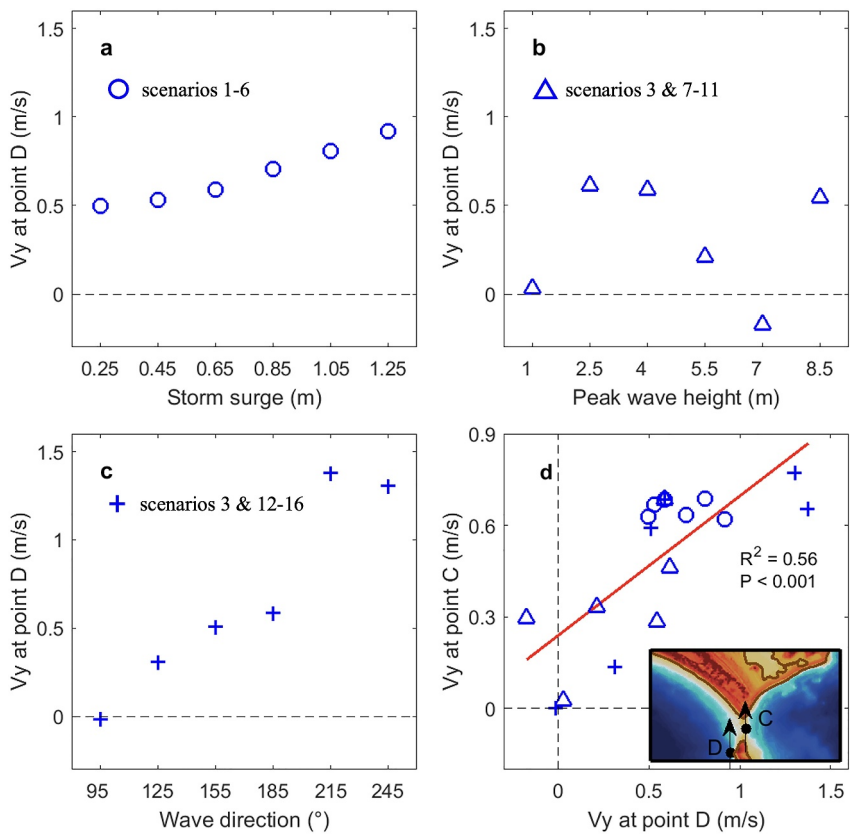

Figure 11. Relationship between the northward velocity along the west side of Gooseberry Island and the northward velocity component across the tombolo. Northward velocity at point D as a function of storm parameters, including storm surge (a), peak wave height (b) and wave direction (c), respectively. Correlation between the northerly velocity across the tombolo and the northerly velocity at point D (d). The coefficient of determination (R^2) and p value for the linear regression are annotated. Data points presented here are computed at the peak of the storm surge.

wave-breaking zone closer to the shore. Previous studies also suggest that larger waves shift the circulation cell seaward, reducing nearshore currents (Mouragues et al., 2020). This phenomenon is also observed in our results indicated by the blue triangles in Figure 11b. However, we further propose that a potential expansion of the velocity field around the circulation cell occurs simultaneously with the seaward shift (Figure 7a vs. Figure 7g). For example, in the "Wave +" scenario, the expansion of the velocity field around the circulation cells amplifies the nearshore current in the west side of the tombolo and East Beach (Figure 7b vs. Figures 7h and 11b).

In addition to the effects of storm surge and wave height, wave direction is a critical factor in modulating circulation currents. Previous studies found that the amount of wave energy reaching the shoreline and subsequent energy dissipation are highly dependent on the direction of wave propagation (Han et al., 2021; Hsu et al., 2006). In our study area, shallow zones around islands and bedrock shoals act as regions of high wave energy dissipation. When waves approach perpendicular to the shoreline, two symmetrical circulation cells form (Figure 7a). However, when waves propagate obliquely, the circulation cells become asymmetrical (Figure 7e). This phenomenon supports findings from prior studies, where oblique wave input around headlands generates asymmetrical current patterns (George et al., 2019; Klein et al., 2020; McCarroll et al., 2018). Landward migration of the west circulation cell amplifies the velocity on the west domain, as observed in the scenario with a wave direction of 215° or 245° in Figure 11c. Furthermore, we show that the northward flow across the tombolo is primarily influenced by the circulation cell on the west domain (Figure 11d).

4.2. Horizontal and Vertical Bottom Sediment Grain Size Distribution Influence Sediment Movement Across the Tombolo

Our model shows that the primary direction of sediment movement is west to east, whereas little sediment moves in the opposite direction (Figure 8). The transport of sediment from west to east is dependent on two key factors: (a) the strength and path of the current, and (b) bottom sediment grain size distribution in both horizontal and vertical dimensions. Several numerical studies have incorporated spatial variations in sediment composition within the seabed to achieve accurate sediment transport estimates (Guillou & Chapalain, 2010; Huisman et al., 2018). This consideration is crucial as finer sediment particles typically exhibit greater transport potential than coarser ones (Andualem et al., 2023; McLaren & Bowles, 1985). Coastal areas characterized by mixed sediment and rocky surfaces have received limited attention in transport studies due to their complexity (Trenhaile, 2016). Moreover, an accurate identification of rocky areas is critical to prevent overestimation of sediment transport (Xie et al., 2024). In the reference scenario of our study, the prevailing currents originate from the west side of Gooseberry Island (Figure 7b). However, this beach is predominantly rocky (Figures 3a and 3b) and there is limited sand in the nearshore to be resuspended and transported to the east domain (Figure 8).

In contrast, in scenarios characterized by a large wave environment or waves coming from the southwest, there is an increase in water level difference, intensifying the cross-tombolo velocities (Figure 9). Given that the sediment composition in the west domain is predominantly gravel and sand, stronger currents result in a noticeable increase in the potential sediment transport to the east domain (Figure 8). This also explains why Hurricane Bob exhibited a smaller peak sediment flux than Hurricane Irene, which had a more oblique wave angle, despite both having identical peak wave heights (Figure 8a). More specifically, the wave direction for Hurricane Irene during peak wave height is ~190°, compared to roughly 180° for Hurricane Bob (Figures 5e and 5g). Hurricane Irene produced strong longshore currents capable of transporting gravel and sand from the western Horseneck Beach to East Beach, whereas Hurricane Bob generated currents originating from the rocky western side of Gooseberry Island (Figure S9 in Supporting Information S1). This is because Hurricane Irene was dominated by large wave heights, similar to the "Wave +" scenario (Figures 7g and 7h vs. Figures S9a and S9b in Supporting Information S1), whereas Hurricane Bob was characterized by both large storm waves and a significant storm surge, generating a current pattern more similar to the "Surge +" scenario (Figures 7c and 7d vs. Figures S9c and S9d in Supporting Information S1). This difference is noteworthy, especially considering that Hurricane Bob created a higher storm surge compared to Hurricane Irene (Figures 5d and 5f).

In addition to the impact of horizontal sediment grain size distribution, their vertical distribution could also affect the amount of sediment deposition on East Beach. In this study, we incorporated a two-layer sediment profile to mimic the vertical sediment gradient observed in the field (Figure 3) and in previous studies (FitzGerald et al., 1992). Gravel is more resistant to movement, so the transported sediment is mostly sand (Figure S10 in Supporting Information S1). Although the general erosion and deposition patterns are similar regardless of the

initial sediment layer thickness, a thinner sand layer reduces the total sediment deposition along East Beach (Figure S11 in Supporting Information S1). For instance, a 25-cm sand layer may result in less sediment deposition compared to the current model setting with a 50-cm sand layer (Figure S11d in Supporting Information S1). Conversely, increasing the initial sand thickness does not significantly alter the sand deposition in the east domain (Figure S11e in Supporting Information S1). For more accurate estimations of sediment deposition along East Beach, future studies should incorporate precise measurements of sediment layer thickness.

4.3. Source-To-Sink Sediment Movement Driven by Circulation Cells

To better understand the specific role of sediment distribution in sediment transport rates across the tombolo, we first identify locations where sediment deposition occurs in the east domain. Then, we quantify changes in sediment volume for the respective sediment compositions in the eastern beach region (Figure 12). Our analysis suggests that during storms, sediment in the western domain is transported across the tombolo and deposited along the eastern shoreline near the tombolo (Figures 12a–12g). Under typical storm conditions, whether idealized storms or those occurring annually (e.g., Extratropical Storm Elliott), west domain sediment only leads to relatively thin deposition along a narrow nearshore area having an average thickness of less than 10 cm (Figures 12a and 12e). The limited amount of sediment transported across the tombolo during the reference storm agrees with previous modeling studies (Tsai et al., 2023). In contrast, during extreme storms or when waves come from the southwest, deposition increases to around 20 cm (Figures 12c, 12d and 12f, 12g). The high rate of sediment deposition highlights the significance of wave height and wave direction on the sediment transport regime across the tombolo, as demonstrated in prior research by Malliouri et al. (2022). Moreover, the impact of tidal currents on sediment transport is minimal in this wave-dominated system (Figure S12 in Supporting Information S1). However, in areas where tidal currents are strong, especially near tidal inlets, ebb tidal currents can counteract circulation cells, move sediment offshore and contribute to the formation of offshore sandbars (Siegle et al., 2004, 2007).

We have further calculated changes in sediment volume in East Beach region resulting from the deposition of sediment from the west domain and local erosion (Figure 12h). We find that existing sediment on East Beach is eroded during storms (depicted by the green bars in Figure 12h), which aligns with previous observations and numerical studies, where storms erode sediment at the beach face (Brenner et al., 2018; Palinkas et al., 2014). We further show that sediment erosion from East Beach increases with storm surge, wave height, and waves from the

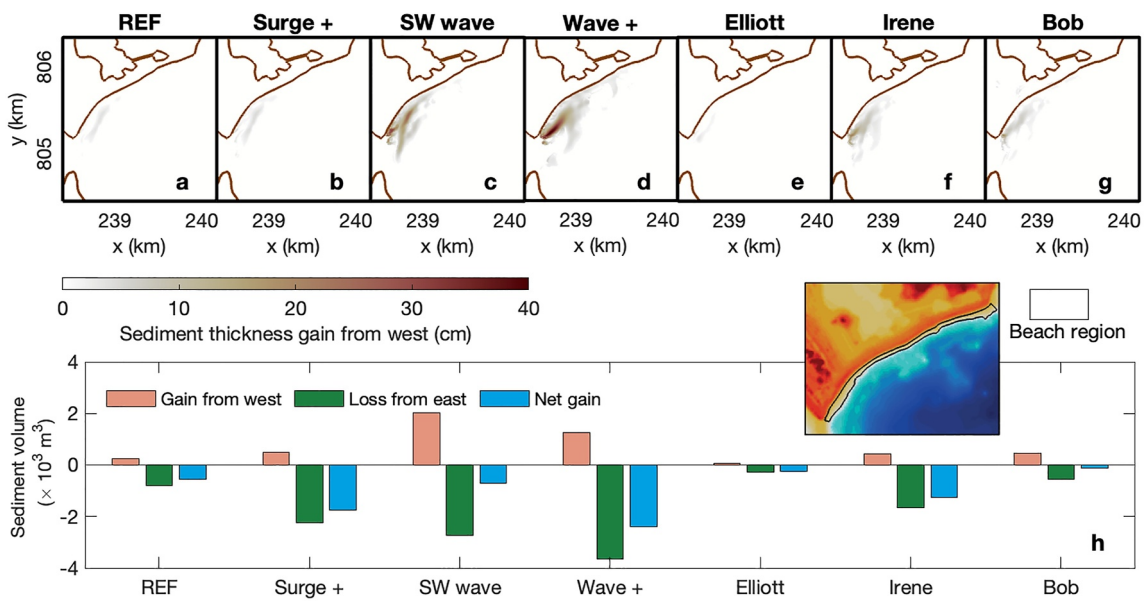

Figure 12. Variations in sediment thickness in the east domain. Spatial distribution of sediment thickness resulting from sediment transported from the west domain (a–g). The bottom bar plot illustrates the sediment volume gained from west sediments, sediment volume lost from East Beach, and the net sediment volume change (i.e., gain from west minus loss from east). These calculations are based on the east beach region, as per previous studies (Xie et al., 2024). The seaward water depth of the beach region is set to 2 m.

southwest (Figure 12h). Sediment from the west domain can only partially offset sediment loss (Figure 12). Previous studies have quantified storm erosion of beach sediment, but here we demonstrate that human activity, such as causeway removal, has the potential to exacerbate sediment erosion from East Beach region (Figure 13). More specifically, while removing the causeway would enhance sediment contribution to East Beach from Horseneck Beach (Figures 12a–12g), the additional longshore (along the shore of Gooseberry Island and the tombolo) currents across the tombolo (Figure 13c) would increase sediment erosion to the western end of East Beach (see blue area near the tombolo in Figure 13f). The eroded sediment is likely deposited nearby (see brown area near the tombolo in Figure 13f). This suggests that variations in sediment thickness near the tombolo are sensitive to the causeway removal.

Our results show that erosion primarily occurs in the areas offshore of Gooseberry Island where the substrate consists of erodible sediment, while sedimentation takes place onshore of these eroded areas (Figure S13 in Supporting Information S1). These patterns are likely driven by the circulation cells on the two sides of Gooseberry Island, which move sediment onshore by sourcing offshore sandy areas (Siegle et al., 2007). Although there are no large sandbars in our study site, onshore currents from circulation cells could potentially erode sand from these sandbars and redistribute it along the shorelines (Figure 7). This process can not only affect LST and the formation of salients/tombolos but also alter the shape of offshore sandbars (Siegle et al., 2004, 2007).

In our modeling work, we focused on sediment volume in East Beach during a single storm. It is important to note that sediment may also move back onshore during the fair weather season, potentially restoring the sediment lost from the beach (Aagaard et al., 2012; Dubois, 1988; Roberts et al., 2013). Beach recovery mainly occurs within the active beach profile, which extends to the depth of closure including the upper shoreface. Beyond this depth, coastal morphological changes due to wave impacts are observed to remain limited (Hallermeier, 1978). The depth of closure of East Beach is approximately 8 m, according to our previous study (Xie et al., 2024), and was calculated based on annual hourly wave data recorded at the buoy station (Figure 1a). A net sediment gain is found when considering a larger region with an 8-m water depth (see the blue bars in Figures S14 and S15 in Supporting Information S1). Here the incoming west sediments exceed sediment losses (orange bars vs. green bars in Figures S14 and S15 in Supporting Information S1). This is because sediment from the west domain is primarily deposited on the upper shoreface of the east domain, as shown in Figures 12a–12g. Future studies should also investigate the residence time of sediment transported into the east domain across the tombolo along with the associated morphological changes, especially considering the impact of consecutive storms (Vousdoukas et al., 2012).

4.4. Additional Processes Affecting Sediment Transport Across the Tombolo and Future Research Directions

We further explored the effect of the wave period on sediment transport. We found that an increase in wave period enhances the peak sediment flux (Figure S16a in Supporting Information S1), which eventually leads to a higher

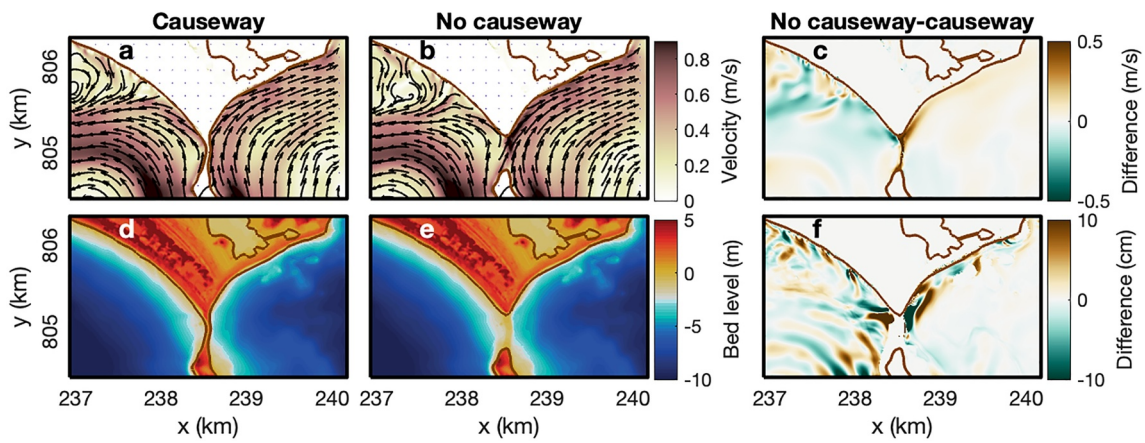

Figure 13. Comparison of velocity field and bed level between scenarios with and without causeway. Velocity field during peak wave height (a–b) and their difference (c). Bed level at the end of simulation (d–e) and their difference (f). Results displayed here are based on the REF (scenario 3).

total sediment transport, particularly from the west domain to the east domain (Figure S16b in Supporting Information S1). This aligns with early findings that longer wave periods (swell waves) can increase sediment transport capacity by altering bottom orbital velocity (Jing & Ridd, 1996; Zhang et al., 2009). Larger wave heights result in higher sediment flux and total sediment transport regardless of wave period (REF scenario vs. Wave + scenario in Figure S16 in Supporting Information S1). Another important process, local wind-wave generation, is not considered in the model simulations. This is to avoid overestimation of wave heights when applying spatially uniform wind fields over the entire domain (Figure S17 in Supporting Information S1). This could likely be improved by using spatially varying wind fields, particularly near the coastline (Huang et al., 2013). Given that our domain has a limited wind fetch, excluding local wind waves still allows us to produce relatively reasonable wave fields (Figure S17b in Supporting Information S1). However, for larger domains on a continental scale, incorporating wind-wave generation is crucial for providing accurate wave height distributions (Huang et al., 2013; Wornom et al., 2001).

In addition, Delft3D-WAVE employs SWAN for wave propagation to the coast, which has been widely used for its robustness in simulating wave transformation processes such as refraction, shoaling, and breaking (George et al., 2019; Huisman et al., 2018; King et al., 2021). However, SWAN has known limitations in simulating wave diffraction, particularly around headlands and other complex coastal features (SWAN, 2015). SWAN can properly account for diffraction if the grid size is refined to less than 1/10-1/5 of the wavelength (SWAN, 2015). This necessitates a very fine wave grid, especially for storm events with short wavelengths. The wavelength around the causeway ranges between 50 and 200 m and increases with storm wave height and storm surge (Figure S18 in Supporting Information S1). Our grid resolution (40 m) may provide a relatively accurate evaluation of wave diffraction during severe storm events such as Hurricane Bob but may fail to do so during typical storm events such as the recent Extratropical Storm Elliott. This limitation could potentially lead to an underestimation of wave energy distribution, particularly on the downdrift side of the system, given that the dominant waves in our study area come from the south to the southwest. This inaccuracy could ultimately affect wave attenuation and set-up, and subsequently influence the amount of sediment flux across the tombolo. Future studies could benefit from incorporating models with enhanced diffraction capabilities or using hybrid approaches that combine SWAN with other modules that better represent diffraction processes, thereby improving accuracy in such complex coastal environments (Kim et al., 2017; Lin, 2013).

Our model solves the depth-averaged shallow water equations; however, the three-dimensional effects might play an important role in sediment transport. For example, the potential impacts of offshore-directed undertow currents arising from set-up gradients during storms are neglected. Undertow currents could displace beach sediment offshore, facilitating the formation of offshore sandbars (Mariño-Tapia et al., 2004). Changes in wave period could also affect three-dimensional wave propagation processes such as wave-induced turbulence, shoaling, refraction, and diffraction, subsequently modifying sediment transport patterns (Sierra & Casas-Prat, 2014; Toffoli et al., 2012). Future modeling research should investigate the interactions of circulation cells with the three-dimensional flow field (Franz et al., 2017).

The model simulations were based on a modified bathymetry, where the current causeway was lowered followed by a long-term simulation to obtain an equilibrium state (Figures 1d and 1e). The historical morphology of the tombolo, which was documented in 1892, was used as a reference to lower the causeway. However, over the past 130 years, potential impacts of climate change such as sea-level rise have likely influenced the tombolo morphology. The conditions for forming a submerged tombolo occurred during a slow rise and subsequent stagnation of sea level in the Holocene (Benac et al., 2019). Nevertheless, accelerated rising sea levels along with larger and more frequent storms could erode and submerge the tombolo (Vu et al., 2018). Given the uncertain future of the tombolo under climate change, it is reasonable for our models to approximate the tombolo elevation based on historical maps. Future research could explore how climate change affects tombolo evolution, particularly under projected sea-level rise and increased storm activity (Emanuel, 2017; Goddard et al., 2015).

5. Conclusions

Our numerical simulations reveal that sediment transport across a tombolo is largely governed by circulation cells on both sides of the tombolo. These circulation cells, which form due to wave energy dissipation during storms, play a critical role in determining the patterns of hydrodynamics and sediment dynamics across the tombolo. Sediment transport across the tombolo only occurs during very large storms (e.g., with an 8-m offshore wave

height). In typical storm scenarios with waves coming from the south, predominant currents are observed from the west side of the offshore island flushing toward the beach on the downdrift side. This current strength intensifies when waves approach from the southwest, causing a landward migration of the west circulation cell. However, the offshore of the island is predominantly rocky, limiting the amount of sediment that can be resuspended and transported across the tombolo.

Our results indicate that the existence of offshore islands shelters the east domain, resulting in lower wave energy and less wave dissipation on the east compared to the west side of the tombolo. During extreme storms, this imbalance increases water level differences between the two sides, which, in turn, creates west to east flow across the tombolo. In addition, the northward component of velocity from along the island across the tombolo is determined by the position, magnitude, and size of the two circulation cells. Under common storm wave conditions, with waves from the south, the circulation cells are symmetrical. However, as the wave height increases, the circulation cells shift offshore, expanding the velocity field of the east circulation cell and creating strong currents along the eastern shoreline. Conversely, when waves approach from the southwest, the west cell moves closer to the shore while the east cell moves offshore, enhancing currents across the tombolo. Although removing the anthropogenic structures such as causeway would facilitate sediment transport across the tombolo during large storms, it should be noted that the same storm waves also increase erosion along the downdrift beach. As a result, the amount of sediment from the west domain reaching the east domain may not fully offset storm-induced sediment losses.

Data Availability Statement

The wave data are collected from an offshore buoy station (Station No.: BUZM3 & 44085) maintained by the National Data Buoy Center (NDBC, 2023). The historical tidal level is retrieved from the Newport tidal gauge (Station No.: 8452660) operated by NOAA (NOAA, 2023). The sediment texture map indicating the spatial sediment types within the Western Buzzards Bay is obtained from USGS (Foster, 2014). Storm surge, peak wave height and wave direction of 100 historical storm events are obtained from a regional modeling data set by the NACCS Coastal Hazards System (Cialone et al., 2015). Delft3D is an open-source code available online (Deltares, 2014).

Acknowledgments
Funding for this project was gratefully received from the Buzzards Bay Coalition through a grant from The Rathmann Family Foundation.

References

Aagaard, T., Hughes, M., Baldock, T., Greenwood, B., Kroon, A., & Power, H. (2012). Sediment transport processes and morphodynamics on a reflective beach under storm and non-storm conditions. *Marine Geology*, *326*, 154–165. https://doi.org/10.1016/j.margeo.2012.09.004

Andualem, T. G., Hewa, G. A., Myers, B. R., Peters, S., & Boland, J. (2023). Erosion and sediment transport modeling: A systematic review. *Land*, *12*(7), 1396. https://doi.org/10.3390/land12071396

Bacon, J., Vincent, C., Dolphin, T., Taylor, J., Pan, S., & O'Connor, B. (2007). Shore-parallel breakwaters in meso-tidal conditions: Tidal controls on sediment transport and their longer term, regional impacts at sea Palling, UK. *Journal of Coastal Research*, 369–373.

Bai, X., Jiang, H., Li, C., & Huang, L. (2020). Joint probability distribution of coastal winds and waves using a log-transformed kernel density estimation and mixed copula approach. *Ocean Engineering*, *216*, 107937. https://doi.org/10.1016/j.oceaneng.2020.107937

Benac, Č., Bočić, N., & Ružić, I. (2019). On the origin of both a recent and submerged tombolo on Prvić Island in the Kvarner area (Adriatic Sea, Croatia). *Geologia Croatica*, *72*(3), 195–203. https://doi.org/10.4154/gc.2019.14

Bent, G. C. (1995). *Streamflow, ground-water recharge and discharge, and characteristics of surficial deposits in Buzzards Bay Basin, Southeastern Massachusetts*. US Geological Survey.

Booij, N., Ris, R. C., & Holthuijsen, L. H. (1999). A third-generation wave model for coastal regions: 1. Model description and validation. *Journal of Geophysical Research*, *104*(C4), 7649–7666. https://doi.org/10.1029/98JC02622

Brenner, O. T., Lentz, E. E., Hapke, C. J., Henderson, R. E., Wilson, K. E., & Nelson, T. R. (2018). Characterizing storm response and recovery using the beach change envelope: Fire Island, New York. *Geomorphology*, *300*, 189–202. https://doi.org/10.1016/j.geomorph.2017.08.004

Butt, T., Russell, P., Miles, J., & Turner, I. (2000). Hydrodynamics and cross-shore sediment transport in the swash-zone of natural beaches: A review. *Journal of Coastal Research*, *50*(sp1), 255–268. https://doi.org/10.2112/jcr-si50-120.1

Cheung, K. F., Tang, L., Donnelly, J. P., Scileppi, E. M., Liu, K. B., Mao, X. Z., et al. (2007). Numerical modeling and field evidence of coastal overwash in southern New England from Hurricane Bob and implications for paleotempestology. *Journal of Geophysical Research*, *112*(F3). https://doi.org/10.1029/2006jf000612

Chi, S., Zhang, C., & Zheng, J. (2023). Sandy shoreline recovery ability after breakwater removal. *Frontiers in Marine Science*, *10*, 1191386. https://doi.org/10.3389/fmars.2023.1191386

Chowdhury, P., Behera, M. R., & Reeve, D. E. (2020). Future wave-climate driven longshore sediment transport along the Indian coast. *Climatic Change*, *162*(2), 405–424. https://doi.org/10.1007/s10584-020-02693-7

Cialone, M. A., Massey, T. C., Anderson, M. E., Grzegorzewski, A. S., Jensen, R. E., Cialone, A., et al. (2015). North Atlantic coast comprehensive study (NACCS) coastal storm model simulations: Waves and water levels (Version 2.0) [Software]. *U.S. Army Corps of Engineers*. https://chs.erdc.dren.mil/Home/Index

CIRES. (2014). Cooperative institute for research in environmental sciences (CIRES) at the University of Colorado, boulder. Continuously updated digital elevation model (CUDEM) - 1/9 arc-second resolution bathymetric-topographic tiles. In *NOAA national centers for environmental information*.

Clamflats. (2019). Old postcards and photos of Westport, Mass. And surroundings (Version 1) [Dataset]. *PBase*. https://pbase.com/clamflats/gooseberry_bar_rock

Cuadrado, D. G., Gómez, E. A., & Ginsberg, S. S. (2005). Tidal and longshore sediment transport associated to a coastal structure. *Estuarine, Coastal and Shelf Science*, *62*(1), 291–300. https://doi.org/10.1016/j.ecss.2004.09.010

da Silva, A. P., da Silva, G. V., Strauss, D., Murray, T., Woortmann, L. G., Taber, J., et al. (2021). Headland bypassing timescales: Processes and driving forces. *Science of the Total Environment*, *793*, 148591. https://doi.org/10.1016/j.scitotenv.2021.148591

Deltares. (2014). Simulation of multi-dimensional hydrodynamic flows and transport phenomena, including sediments (Version 3.15.34158) [Software]. *Deltares*. https://oss.deltares.nl/

Dodet, G., Melet, A., Ardhuin, F., Bertin, X., Idier, D., & Almar, R. (2019). The contribution of wind-generated waves to coastal sea-level changes. *Surveys in Geophysics*, *40*(6), 1563–1601. https://doi.org/10.1007/s10712-019-09557-5

Dubois, R. N. (1988). Seasonal changes in beach topography and beach volume in Delaware. *Marine Geology*, *81*(1–4), 79–96. https://doi.org/10.1016/0025-3227(88)90019-9

Dullaart, J. C., Muis, S., De Moel, H., Ward, P. J., Eilander, D., & Aerts, J. C. (2023). Enabling dynamic modelling of coastal flooding by defining storm tide hydrographs. *Natural Hazards and Earth System Sciences*, *23*(5), 1847–1862. https://doi.org/10.5194/nhess-23-1847-2023

Emanuel, K. (2017). Will global warming make hurricane forecasting more difficult? *Bulletin of the American Meteorological Society*, *98*(3), 495–501. https://doi.org/10.1175/bams-d-16-0134.1

Fagherazzi, S., Mariotti, G., Leonardi, N., Canestrelli, A., Nardin, W., & Kearney, W. S. (2020). Salt marsh dynamics in a period of accelerated sea level rise. *Journal of Geophysical Research: Earth Surface*, *125*(8), e2019JF005200. https://doi.org/10.1029/2019JF005200

FitzGerald, D. M., Baldwin, C. T., Ibrahim, N. A., & Humphries, S. M. (1992). Sedimentologic and morphologic evolution of a beach ridge barrier along an indented coast: Buzzards Bay, Massachusetts. *Quaternary Coasts of the United States*, 65–75. https://doi.org/10.2110/pec.92.48.0065

FitzGerald, D. M., Baldwin, C. T., Ibrahim, N. A., & Sand, D. R. (1987). Development of the northwestern Buzzards bay shoreline, Massachusetts. In D. M. FitzGerald & P. S. Rosen (Eds.), *Glaciated coasts* (p. 327). Academic Press INC.

FitzGerald, D. M., Hughes, Z. J., Georgiou, I. Y., Black, S., & Novak, A. (2020). Enhanced, climate-driven sedimentation on salt marshes. *Geophysical Research Letters*, *47*(10), e2019GL086737. https://doi.org/10.1029/2019GL086737

Foster, D. S. (2014). Sediment-texture units of the sea floor for Buzzards bay, Massachusetts (BuzzardsBay_sedcover, polygon shapefile, geographic, WGS84) (Version 1) [Dataset]. *USGS*. https://data.usgs.gov/datacatalog/data/USGS:fd6bb70a-1ad6-44b3-9a70-8a6057c3b755

Franz, G., Delpey, M. T., Brito, D., Pinto, L., Leitão, P., & Neves, R. (2017). Modelling of sediment transport and morphological evolution under the combined action of waves and currents. *Ocean Science*, *13*(5), 673–690. https://doi.org/10.5194/os-13-673-2017

Ganju, N. K., Lentz, S. J., Kirincich, A. R., & Farrar, J. T. (2011). Complex mean circulation over the inner shelf south of Martha's Vineyard revealed by observations and a high-resolution model. *Journal of Geophysical Research*, *116*(C10), C10036. https://doi.org/10.1029/2011jc007035

George, D. A., Largier, J. L., Pasternack, G. B., Barnard, P. L., Storlazzi, C. D., & Erikson, L. H. (2019). Modeling sediment bypassing around idealized rocky headlands. *Journal of Marine Science and Engineering*, *7*(2), 40. https://doi.org/10.3390/jmse7020040

Giosan, L., Bokuniewicz, H., Panin, N., & Postolache, I. (1999). Longshore sediment transport pattern along the Romanian Danube delta coast. *Journal of Coastal Research*, 859–871.

Goddard, P. B., Yin, J., Griffies, S. M., & Zhang, S. (2015). An extreme event of sea-level rise along the Northeast coast of North America in 2009–2010. *Nature Communications*, *6*(1), 6346. https://doi.org/10.1038/ncomms7346

Goman, M., Joyce, A., & Mueller, R. (2005). Stratigraphic evidence for anthropogenically induced coastal environmental change from Oaxaca, Mexico. *Quaternary Research*, *63*(3), 250–260. https://doi.org/10.1016/j.yqres.2005.02.008

Grasso, F., Michallet, H., & Barthélemy, E. (2011). Experimental simulation of shoreface nourishments under storm events: A morphological, hydrodynamic, and sediment grain size analysis. *Coastal Engineering*, *58*(2), 184–193. https://doi.org/10.1016/j.coastaleng.2010.09.007

Greer, M. N., & Madsen, O. S. (1978). Longshore sediment transport data: A review. *Coastal Engineering*, *1978*, 1563–1576. https://doi.org/10.1061/9780872621909.095

Guillou, N., & Chapalain, G. (2010). Numerical simulation of tide-induced transport of heterogeneous sediments in the English Channel. *Continental Shelf Research*, *30*(7), 806–819. https://doi.org/10.1016/j.csr.2010.01.018

Hallermeier, R. J. (1978). Uses for a calculated limit depth to beach erosion. *Coastal Engineering*, *1978*, 1493–1512.

Hamilton, D. G., & Ebersole, B. A. (2001). Establishing uniform longshore currents in a large-scale sediment transport facility. *Coastal Engineering*, *42*(3), 199–218. https://doi.org/10.1016/s0378-3839(00)00059-4

Han, X., Dong, S., & Wang, Y. (2021). Interaction between oblique waves and arc-shaped breakwater: Wave action on the breakwater and wave transformation behind it. *Ocean Engineering*, *234*, 109252. https://doi.org/10.1016/j.oceaneng.2021.109252

Hequette, A., Desrosiers, M., Hill, P. R., & Forbes, D. L. (2001). The influence of coastal morphology on shoreface sediment transport under storm-combined flows, Canadian Beaufort Sea. *Journal of Coastal Research*, 507–516.

Hoque, A., Hossain, N., Ali, S., & Rahman, M. (2019). Wave breaking and bubble formation associate energy dissipation and wave setup. *Ocean Dynamics*, *69*(8), 913–923. https://doi.org/10.1007/s10236-019-01279-x

Hsu, T.-W., Hsu, J. R.-C., Weng, W.-K., Wang, S.-K., & Ou, S.-H. (2006). Wave setup and setdown generated by obliquely incident waves. *Coastal Engineering*, *53*(10), 865–877. https://doi.org/10.1016/j.coastaleng.2006.05.002

Huang, Y., Weisberg, R. H., Zheng, L., & Zijlema, M. (2013). Gulf of Mexico hurricane wave simulations using SWAN: Bulk formula-based drag coefficient sensitivity for Hurricane Ike. *Journal of Geophysical Research: Oceans*, *118*(8), 3916–3938. https://doi.org/10.1002/jgrc.20283

Hubbard, D. K. (1992). Hurricane-induced sediment transport in open-shelf tropical systems; an example from St. Croix, US Virgin Islands. *Journal of Sedimentary Research*, *62*(6), 946–960.

Huisman, B., Ruessink, B., De Schipper, M., Luijendijk, A., & Stive, M. (2018). Modelling of bed sediment composition changes at the lower shoreface of the Sand Motor. *Coastal Engineering*, *132*, 33–49. https://doi.org/10.1016/j.coastaleng.2017.11.007

Idier, D., Bertin, X., Thompson, P., & Pickering, M. D. (2019). Interactions between mean sea level, tide, surge, waves and flooding: Mechanisms and contributions to sea level variations at the coast. *Surveys in Geophysics*, *40*(6), 1603–1630. https://doi.org/10.1007/s10712-019-09549-5

Jing, L., & Ridd, P. V. (1996). Wave-current bottom shear stresses and sediment resuspension in Cleveland Bay, Australia. *Coastal Engineering*, *29*(1–2), 169–186. https://doi.org/10.1016/s0378-3839(96)00023-3

Kaliraj, S., Chandrasekar, N., & Magesh, N. (2014). Impacts of wave energy and littoral currents on shoreline erosion/accretion along the southwest coast of Kanyakumari, Tamil Nadu using DSAS and geospatial technology. *Environmental Earth Sciences*, *71*(10), 4523–4542. https://doi.org/10.1007/s12665-013-2845-6

Kim, G. H., Jho, M. H., & Yoon, S. B. (2017). Improving the performance of SWAN modelling to simulate diffraction of waves behind structures. *Journal of Coastal Research*, *79*(79), 349–353. https://doi.org/10.2112/si79-071.1

King, E. V., Conley, D. C., Masselink, G., Leonardi, N., McCarroll, R. J., Scott, T., & Valiente, N. G. (2021). Wave, tide and topographical controls on headland sand bypassing. *Journal of Geophysical Research: Oceans*, *126*(8), e2020JC017053. https://doi.org/10.1029/2020jc017053

Klein, A. H., da Silva, G. V., Taborda, R., da Silva, A. P., & Short, A. D. (2020). Headland bypassing and overpassing: Form, processes and applications. *Sandy Beach Morphodynamics*, 557–591. https://doi.org/10.1016/b978-0-08-102927-5.00023-0

Kobayashi, N., Agarwal, A., & Johnson, B. D. (2007). Longshore current and sediment transport on beaches. *Journal of Waterway, Port, Coastal, and Ocean Engineering*, *133*(4), 296–304. https://doi.org/10.1061/(asce)0733-950x(2007)133:4(296)

Lavaud, L., Bertin, X., Martins, K., Pezerat, M., Coulombier, T., & Dausse, D. (2022). Wave dissipation and mean circulation on a shore platform under storm wave conditions. *Journal of Geophysical Research: Earth Surface*, *127*(3), e2021JF006466. https://doi.org/10.1029/2021JF006466

Lerma, A. N., Pedreros, R., Robinet, A., & Sénéchal, N. (2017). Simulating wave setup and runup during storm conditions on a complex barred beach. *Coastal Engineering*, *123*, 29–41. https://doi.org/10.1016/j.coastaleng.2017.01.011

Lesser, G. R., Roelvink, J. A., van Kester, J. A. T. M., & Stelling, G. S. (2004). Development and validation of a three-dimensional morphological model. *Coastal Engineering*, *51*(8–9), 883–915. https://doi.org/10.1016/j.coastaleng.2004.07.014

Limber, P. W., Brad Murray, A., Adams, P. N., & Goldstein, E. B. (2014). Unraveling the dynamics that scale cross-shore headland relief on rocky coastlines: 1. Model development. *Journal of Geophysical Research: Earth Surface*, *119*(4), 854–873. https://doi.org/10.1002/2013jf002950

Lin, J.-G. (2013). An improvement of wave refraction-diffraction effect in SWAN. *Journal of Marine Science and Technology*, *21*(2), 198–208.

Longuet-Higgins, M. S. (1970). Longshore currents generated by obliquely incident sea waves: 1. *Journal of Geophysical Research (1896-1977)*, *75*(33), 6778–6789. https://doi.org/10.1029/JC075i033p06778

Ma, H., Xu, L., Okon, S. U., Hu, P., Li, W., Shi, H., & He, Z. (2024). Sediment transport and bed erosion during storm surge using a coupled hydrodynamic and morphodynamic model considering wave and current interaction. *Coastal Engineering*, *187*, 104409. https://doi.org/10.1016/j.coastaleng.2023.104409

Malliouri, D. I., Petrakis, S., Vandarakis, D., Kikaki, K., Hatiris, G.-A., Gad, F.-K., et al. (2022). The role of sea state to the morphological changes of Prasonisi tombolo, Rhodes island, Greece. *Water*, *14*(13), 2016. https://doi.org/10.3390/w14132016

Mangor, K., Drønen, N. K., Kaergaard, K. H., & Kristensen, N. E. (2017). *Shoreline management guidelines*. DHI: Hirschholm.

Mariño-Tapia, I., Aird, N., Davidson, M., Kingston, K., & Ganderton, P. (2004). Tidally modulated sediment transport processes on a shore-attached sandbar. *Journal of Coastal Research*, 395–400.

McCarroll, R. J., Masselink, G., Valiente, N. G., Scott, T., King, E. V., & Conley, D. (2018). Wave and tidal controls on embayment circulation and headland bypassing for an exposed, macrotidal site. *Journal of Marine Science and Engineering*, *6*(3), 94. https://doi.org/10.3390/jmse6030094

McLaren, P., & Bowles, D. (1985). The effects of sediment transport on grain-size distributions. *Journal of Sedimentary Research*, *55*(4), 457–470.

Mouragues, A., Bonneton, P., Castelle, B., Marieu, V., Jak McCarroll, R., Rodriguez-Padilla, I., et al. (2020). High-energy surf zone currents and headland rips at a geologically constrained mesotidal beach. *Journal of Geophysical Research: Oceans*, *125*(10), e2020JC016259. https://doi.org/10.1029/2020jc016259

NDBC. (2023). Wind and wave data collected from national data buoy center (station No.: BUZM3 & 44085) (Version 1) [Dataset]. *NDBC*. https://www.ndbc.noaa.gov/

NOAA. (2023). Historical tidal level data retrieved from Newport tidal gauge under National Oceanic and Atmospheric Administration (station No.:8452660) (Version 1) [Dataset]. *National Oceanic and Atmospheric Administration*. https://tidesandcurrents.noaa.gov/

NOAA. (2024). NOAA's historical map & chart collection (Version 1) [Dataset]. *United States Office of Coast Survey*. https://historicalcharts.noaa.gov/about.php

Nordstrom, K. F. (2014). Living with shore protection structures: A review. *Estuarine, Coastal and Shelf Science*, *150*, 11–23. https://doi.org/10.1016/j.ecss.2013.11.003

Palinkas, C. M., Halka, J. P., Li, M., Sanford, L. P., & Cheng, P. (2014). Sediment deposition from tropical storms in the upper Chesapeake Bay: Field observations and model simulations. *Continental Shelf Research*, *86*, 6–16. https://doi.org/10.1016/j.csr.2013.09.012

Pattiaratchi, C., Hegge, B., Gould, J., & Eliot, I. (1997). Impact of sea-breeze activity on nearshore and foreshore processes in southwestern Australia. *Continental Shelf Research*, *17*(13), 1539–1560. https://doi.org/10.1016/s0278-4343(97)00016-2

Pattiaratchi, C., Olsson, D., Hetzel, Y., & Lowe, R. (2009). Wave-driven circulation patterns in the lee of groynes. *Continental Shelf Research*, *29*(16), 1961–1974. https://doi.org/10.1016/j.csr.2009.04.011

Putnam, J. A., Munk, W. H., & Taylor, M. (1949). The prediction of longshore currents. *Eos, Transactions American Geophysical Union*, *30*(3), 337–345. https://doi.org/10.1029/TR030i003p00337

Roberts, T. M., Wang, P., & Puleo, J. A. (2013). Storm-driven cyclic beach morphodynamics of a mixed sand and gravel beach along the Mid-Atlantic Coast, USA. *Marine Geology*, *346*, 403–421. https://doi.org/10.1016/j.margeo.2013.08.001

Roy, P., Cowell, P., Ferland, M., & Thom, B. (1994). Wave-dominated coasts. *Coastal evolution: Late Quaternary shoreline morphodynamics*, 121–186. https://doi.org/10.1017/cbo9780511564420.006

Sankaranarayanan, S. (2007). Modeling the tide and wind-induced circulation in Buzzards Bay. *Estuarine, Coastal and Shelf Science*, *73*(3–4), 467–480. https://doi.org/10.1016/j.ecss.2006.12.022

Shetty, A., & Jayappa, K. (2020). Seasonal variation in longshore sediment transport rate and its impact on sediment budget along the wave-dominated Karnataka coast, India. *Journal of Earth System Science*, *129*, 1–14. https://doi.org/10.1007/s12040-020-01504-y

Siegle, E., Huntley, D. A., & Davidson, M. A. (2004). Physical controls on the dynamics of inlet sandbar systems. *Ocean Dynamics*, *54*(3–4), 360–373. https://doi.org/10.1007/s10236-003-0062-7

Siegle, E., Huntley, D. A., & Davidson, M. A. (2007). Coupling video imaging and numerical modelling for the study of inlet morphodynamics. *Marine Geology*, *236*(3–4), 143–163. https://doi.org/10.1016/j.margeo.2006.10.022

Sierra, J., & Casas-Prat, M. (2014). Analysis of potential impacts on coastal areas due to changes in wave conditions. *Climatic Change*, *124*(4), 861–876. https://doi.org/10.1007/s10584-014-1120-5

Specht, C., Lewicka, O., Specht, M., Dąbrowski, P., & Burdziakowski, P. (2020). Methodology for carrying out measurements of the tombolo geomorphic landform using unmanned aerial and surface vehicles near Sopot Pier, Poland. *Journal of Marine Science and Engineering*, *8*(6), 384. https://doi.org/10.3390/jmse8060384

Sun, Y., Chen, C., Beardsley, R. C., Xu, Q., Qi, J., & Lin, H. (2013). Impact of current-wave interaction on storm surge simulation: A case study for hurricane Bob. *Journal of Geophysical Research: Oceans*, *118*(5), 2685–2701. https://doi.org/10.1002/jgrc.20207

Svendsen, I. A. (1984). Wave heights and set-up in a surf zone. *Coastal Engineering*, *8*(4), 303–329. https://doi.org/10.1016/0378-3839(84)90028-0

SWAN, S. (2015). *Technical documentation (SWAN Cycle III version 41.01 A)*. Delft University of Technology.
Toffoli, A., McConochie, J., Ghantous, M., Loffredo, L., & Babanin, A. V. (2012). The effect of wave-induced turbulence on the ocean mixed layer during tropical cyclones: Field observations on the Australian North-West Shelf. *Journal of Geophysical Research*, *117*(C11). https://doi.org/10.1029/2011jc007780
Trenhaile, A. (2016). Rocky coasts —— Their role as depositional environments. *Earth-Science Reviews*, *159*, 1–13. https://doi.org/10.1016/j.earscirev.2016.05.001
Tsai, C.-P., Chen, Y.-C., & Ko, C.-H. (2023). Prediction of bay-shaped shorelines between detached breakwaters with various gap spacings. *Sustainability*, *15*(7), 6218. https://doi.org/10.3390/su15076218
van Rijn, L. C., Walstra, D. J. R., & Ormondt, M. (2004). Description of TRANSPOR2004 and implementation in Delft3D-online. Z3748.
van Wiechen, P., de Vries, S., Reniers, A., & Aarninkhof, S. (2023). Dune erosion during storm surges: A review of the observations, physics and modelling of the collision regime. *Coastal Engineering*, *186*, 104383. https://doi.org/10.1016/j.coastaleng.2023.104383
Vieira da Silva, G., Toldo Jr, E. E., Klein, A. H. D. F., & Short, A. D. (2018). The influence of wave-wind- and tide-forced currents on headland sand bypassing – Study case: Santa Catarina Island north shore, Brazil. *Geomorphology*, *312*, 1–11. https://doi.org/10.1016/j.geomorph.2018.03.026
Villarini, G., Vecchi, G. A., Knutson, T. R., & Smith, J. A. (2011). Is the recorded increase in short-duration North Atlantic tropical storms spurious? *Journal of Geophysical Research*, *116*(D10), D10114. https://doi.org/10.1029/2010jd015493
Vincent, C. E., Young, R. A., & Swift, D. J. (1983). Sediment transport on the long island shoreface, north American Atlantic shelf: Role of waves and currents in shoreface maintenance. *Continental Shelf Research*, *2*(2–3), 163–181. https://doi.org/10.1016/0278-4343(83)90014-6
Vousdoukas, M. I., Almeida, L. P. M., & Ferreira, Ó. (2012). Beach erosion and recovery during consecutive storms at a steep-sloping, meso-tidal beach. *Earth Surface Processes and Landforms*, *37*(6), 583–593. https://doi.org/10.1002/esp.2264
Vu, M., Lacroix, Y., & Nguyen, V. (2018). Investigating the effects of sea-level rise on morphodynamics in the western Giens tombolo, France. *IOP Conference Series: Earth and Environmental Science*, *167*, 012027. https://doi.org/10.1088/1755-1315/167/1/012027
Wang, K., Hou, Y., Li, S., Du, M., Chen, J., & Lu, J. (2020). A comparative study of storm surge and wave setup in the East China Sea between two severe weather events. *Estuarine, Coastal and Shelf Science*, *235*, 106583. https://doi.org/10.1016/j.ecss.2020.106583
Warner, J. C., Geyer, W. R., & Lerczak, J. A. (2005). Numerical modeling of an estuary: A comprehensive skill assessment. *Journal of Geophysical Research*, *110*(C5), C05001. https://doi.org/10.1029/2004jc002691
Willmott, C. J. (1981). On the validation of models. *Physical Geography*, *2*(2), 184–194. https://doi.org/10.1080/02723646.1981.10642213
Woodworth, P. L., Melet, A., Marcos, M., Ray, R. D., Wöppelmann, G., Sasaki, Y. N., et al. (2019). Forcing factors affecting sea level changes at the coast. *Surveys in Geophysics*, *40*(6), 1351–1397. https://doi.org/10.1007/s10712-019-09531-1
Wornom, S. F., Welsh, D. J., & Bedford, K. W. (2001). On coupling the SWAN and WAM wave models for accurate nearshore wave predictions. *Coastal Engineering Journal*, *43*(03), 161–201. https://doi.org/10.1142/s0578563401000335
Xie, D., Hughes, Z., FitzGerald, D., Tas, S., Asik, T. Z., & Fagherazzi, S. (2024). Impacts of climate change on coastal hydrodynamics around a headland and potential headland sediment bypassing. *Geophysical Research Letters*, *51*(4), e2023GL105323. https://doi.org/10.1029/2023GL105323
Yang, S., Bouma, T. J., Xu, K., Shi, B., Yang, H., Zhang, W., et al. (2023). Storms dominate the erosion of the Yangtze Delta and southward sediment transport. *Science Bulletin*, *68*(6), 553–556. https://doi.org/10.1016/j.scib.2023.03.005
Yasso, W. E. (1965). Plan geometry of headland-bay beaches. *The Journal of Geology*, *73*(5), 702–714. https://doi.org/10.1086/627111
Zhang, Q.-H., Bing, Y., & Onyx, W. (2009). Fine sediment carrying capacity of combined wave and current flows. *International Journal of Sediment Research*, *24*(4), 425–438. https://doi.org/10.1016/s1001-6279(10)60015-7
Zhang, Z., Chen, C., Song, Z., Zhang, D., Hu, D., & Guo, F. (2020). A FVCOM study of the potential coastal flooding in apponagansett bay and clarks cove, Dartmouth Town (MA). *Natural Hazards*, *103*(3), 2787–2809. https://doi.org/10.1007/s11069-020-04102-9
Zhou, Z., Wu, Y., Fan, D., Wu, G., Luo, F., Yao, P., et al. (2022). Sediment sorting and bedding dynamics of tidal flat wetlands: Modeling the signature of storms. *Journal of Hydrology*, *610*, 127913. https://doi.org/10.1016/j.jhydrol.2022.127913
Zhu, Q., & Wiberg, P. L. (2022). The importance of storm surge for sediment delivery to microtidal marshes. *Journal of Geophysical Research: Earth Surface*, *127*(9), e2022JF006612. https://doi.org/10.1029/2022jf006612